Multiple correlation lengths and type-1.5 superconductivity in $U(1)$ superconductors due to hidden competition between irreducible representations of nonlocal pairing

Anton Talkachov [1,*] Paul Leask [1] and Egor Babaev [1,2]
[1]*Department of Physics, KTH-Royal Institute of Technology, SE-106 91 Stockholm, Sweden*
[2]*Wallenberg Initiative Materials Science for Sustainability, Department of Physics, KTH Royal Institute of Technology, SE-106 91 Stockholm, Sweden*

(Received 23 November 2025; revised 19 March 2026; accepted 11 May 2026; published 18 June 2026)

The ratio of magnetic field penetration length λ and superconducting coherence length ξ is a defining quantity that governs magnetic response and underpins the conventional type-I and type-II classification of superconductors. While multicomponent superconductors are known to exhibit multiple coherence lengths with rich and often exotic behavior, single-component superconductors are traditionally assumed to be fully characterized by a single Ginzburg-Landau parameter. Here we revisit this concept. We demonstrate that even nominally single-component superconductors are, in general, intrinsically characterized by multiple coherence lengths. Specifically, we analyze a common physical situation in which a subdominant pairing channel is fully suppressed in the ground state, yielding a nominally single-component superconducting ground state. We show that, nonetheless, proximity to a competing pairing instability generically gives rise to multiple correlation lengths with a nontrivial hierarchy. This has consequences for all inhomogeneous states. Especially near a competing pairing instability, the magnetic field penetration depth lies between two distinct coherence lengths, leading to a breakdown of the conventional type-I and type-II dichotomy and enabling the coexistence of vortex clusters and Meissner domains. More broadly, we find that superconducting states cannot, in general, be classified by a single fundamental length scale, even in ostensibly conventional single-component systems.

DOI: 10.1103/bf2v-wtkt

I. INTRODUCTION

The coherence length, introduced by Ginzburg and Landau [1], is a key characteristic of a superconducting state. It is defined as an exponent that characterizes the spatial recovery of the Cooper pairing field away from a perturbation, such as a defect, local density fluctuation, or vortex. In fact, this length scale is the key characteristic not only of a superconducting state but also of the normal state at temperatures close to the phase transition, where it sets the correlation length due to local pairing fluctuations and is important, e.g., in the phenomenon of paraconductivity [2].

Conventionally, superconductors were characterized by a single coherence (or, equivalently, correlation) length. Then its ratio relative to another fundamental length scale, the magnetic field penetration depth λ, determines the magnetic response [3–5]. This is the Ginzburg-Landau (GL) parameter $\kappa = \lambda/\xi$. For $\kappa > 1/\sqrt{2}$, one has a type-II superconductor that possesses stable vortices repelling each other and forming a vortex lattice. In contrast, for $\kappa < 1/\sqrt{2}$ we have a type-I superconductor where vortices attract each other and are not stable.

The clearest exception to this type-I and -II dichotomy is where a superconductor has two broken symmetries, necessitating the introduction of two coherence lengths ξ_1, ξ_2. For example, there are a plethora of superconductors that break $U(1) \times \mathbb{Z}_2$ time-reversal symmetry, giving rise to multiple coherence lengths (see detailed discussion in [6,7]). A new (termed in [8], type-1.5) regime then arises when λ is an intermediate length scale [9]. For a superconductor with n broken symmetries the type-1.5 regime occurs when the magnetic penetration depth λ falls between coherence lengths ξ_i ($\xi_1 < \xi_2 < \cdots \lambda \cdots < \xi_{n-1} < \xi_n$). In such a state, vortices have a composite core with several competing length scales. As a result of this competition, vortices attract each other on the length scale of larger coherence lengths, due to the vortex outer cores overlapping. On length scales of the magnetic penetration depth, the vortices repel one another due to magnetic and current-current interaction, forming stable vortex clusters. This long-range attraction and short-range repulsion behavior, characteristic of type-1.5 superconductivity, enhances the superconducting typology by breaking the type-I and -II dichotomy. A more subtle case is the appearance of multiple correlation lengths in multiband superconductors that break a single $U(1)$ symmetry. In this case, multiple well-defined correlation lengths are not guaranteed by symmetry, but instead require certain microscopic conditions to be met by interband interactions [10–13]. For experimental research see [8,14–17].

In this work, we return to the basic question of what the coherence and correlation lengths and typology of a

*Contact author: anton.talkachov@gmail.com

Published by the American Physical Society under the terms of the Creative Commons Attribution 4.0 International license. Further distribution of this work must maintain attribution to the author(s) and the published article's title, journal citation, and DOI. Funded by Bibsam.

superconducting system with a single broken symmetry are. We consider superconductivity in a system with competing pairing channels that belong to two different irreducible representations of nonlocal pairing. In this case, we specifically focus on the regime where one of the competing order parameters is suppressed. At first glance, such a system represents a case of a single-component superconductor that neither breaks multiple symmetries nor has multiple electronic bands. Nevertheless, we show that, under certain conditions, a suppressed competing pairing channel significantly alters correlations in the system. We show that such a system, in general, can only be described by the introduction of multiple correlation lengths. The origin of additional coherence lengths in this type of ground state comes from the structure of gradient terms.

The effect is partially related to the phenomenon that, in a normal state, a proximate superconducting phase gives rise to well-defined coherence lengths, despite a lack of any broken symmetries. In our case, we find that a proximate, but nondeveloped superconducting phase with different broken symmetry imprints additional correlation lengths in superconducting condensates. We show that this principally alters the type of magnetic response of the system. Furthermore, we show that such a nominally single-component system cannot be a type-II superconductor in proximity to a continuous phase transition to a different pairing state with additional broken symmetry.

We start from a single electronic band microscopic model with nearest-neighbor pairing and compute the phase diagram as a function of doping. Two superconducting components arise in this model from the mathematical concept of symmetry (irreducible representations). Then we derive the corresponding Ginzburg-Landau functional and discuss the coherence lengths ξ_i and magnetic field penetration depth λ. We estimate a region on the phase diagram where type-1.5 superconductivity arises. Performing full scale numerical Ginzburg-Landau calculations, we show the existence of vortex clusters in a $U(1)\times\mathbb{Z}_2$ symmetry-breaking state ($s+id$) and also report configurations with nonzero skyrmion charge. Importantly, we find vortex clusters in the $U(1)$ symmetry-breaking state where *only one* component of the order parameter (s wave or d wave) is nucleated in the ground state.

II. MICROSCOPIC MODEL

Consider a mean-field Hubbard Hamiltonian on a square lattice with attractive interaction V ($V>0$) between nearest neighbors:

$$H_{\mathrm{MF}} = -\sum_{i\sigma}\mu c^{\dagger}_{i,\sigma}c_{i,\sigma} - \sum_{\langle i,j\rangle,\sigma} e^{i\frac{eq}{\hbar}A_{ij}} c^{\dagger}_{i,\sigma}c_{j,\sigma} + \sum_{\langle i,j\rangle}\left(\Delta_{ji}c^{\dagger}_{i,\uparrow}c^{\dagger}_{j,\downarrow} + \Delta^{*}_{ij}c_{i,\downarrow}c_{j,\uparrow} + \frac{|\Delta_{ij}|^2}{V}\right) + \sum_{\substack{\text{plaqu-}\\ \text{ettes}}}\frac{a^2L_z}{2\mu_0 t_{xy}}B_z^2, \tag{1}$$

where $\Delta_{ij} = -V\langle c_{i,\downarrow}c_{j,\uparrow}\rangle$ is the superconducting order parameter on a link ij. Here $c^{\dagger}_{i,\sigma}(c_{i,\sigma})$ is the creation (annihilation) operator for an electron with spin σ on site i, μ is the chemical potential, a is the unit-cell size in xy plane, L_z is the interlayer distance, μ_0 is the vacuum magnetic permeability, and $A_{ij} = \frac{1}{a}\int_j^i \boldsymbol{A}d\boldsymbol{l}$. The energies, gap, chemical potential, and temperature are in the units of hopping integral t_{xy}, and $k_B = 1$.

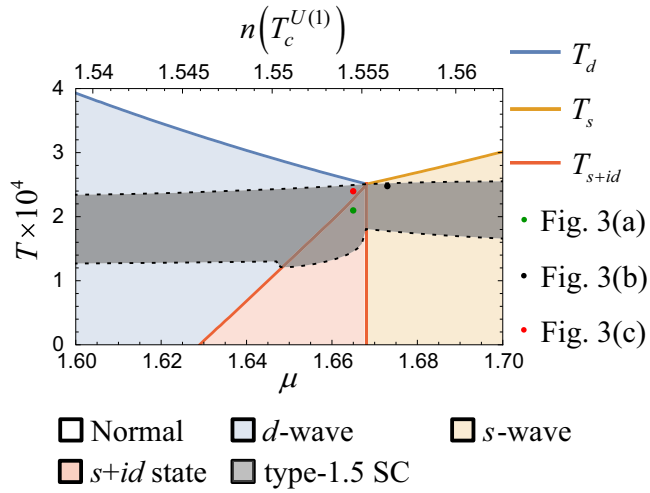


FIG. 1. The phase diagram of the microscopic Hamiltonian (1) in chemical potential μ [or band filling at $U(1)$ critical temperature $n(T_c^{U(1)})$], temperature T coordinates. The region for type-1.5 superconductivity is estimated based on simple approximations described in the text. The green, black, and red points correspond to ($\mu = 1.665$, $T = 2.1\times10^{-4}$), ($\mu = 1.673$, $T = 2.48\times10^{-4}$), and ($\mu = 1.665$, $T = 2.4\times10^{-4}$), respectively. In our microscopic calculations, the parameters we employed are energy cutoff $\omega_D = 0.1$, nearest-neighbor interaction strength $V = 2$. Ginzburg-Landau calculation parameters: unit-cell size $a = 0.4$ nm, interlayer distance $L_z = 1.3$ nm, hopping parameter $t_{xy} = 0.01$ eV.

The superconducting order parameter living on nearest-neighbor links can be mapped to a linear superposition of two one-dimensional irreducible representations living on sites corresponding to extended s wave (A_{1g} irreducible representation) and d wave (B_{1g})

$$\Delta(\boldsymbol{k}) = \Delta_s(\cos k_x + \cos k_y) + \Delta_d(\cos k_x - \cos k_y). \tag{2}$$

Aside from the overall $U(1)$ gauge symmetry, the superconducting gap is characterized by three parameters: the amplitudes $|\Delta_s|$, $|\Delta_d|$, and the relative phase difference between components $\theta = \arg(\Delta_s\Delta_d^*)$. For a state where $|\Delta_s|\neq 0$, $|\Delta_d|\neq 0$, the phase difference is $\pi/2$ for systems with the C_4 rotational symmetry [18–20].

We have computed the superconducting phase diagram in band filling temperature coordinates using numerical solutions of the self-consistency equation for the superconducting gap with small energy cutoff ($\omega_D = 0.1$, see Fig. 1). A d-wave state is preferred near a half-filled band, s wave for an almost filled band, and $s+id$ phase with relative phase difference $\pi/2$ in between. A distinct feature is a sharp (vertical) transition between $s+id$ and s-wave phases, explained in Appendix A. Now, when we know the region of presence of s- and d-wave order parameters, we can investigate the system response to an external magnetic field. We do this in a

Ginzburg-Landau model that is derived in the vicinity of the $U(1)$ phase transition.

III. GINZBURG-LANDAU DESCRIPTION

The Ginzburg-Landau free-energy density, derived from the microscopic model as an expansion in several small parameters associated with two gaps [Eq. (1)] in the weak coupling limit, has the form

$$\begin{aligned} F &= \alpha_1|\Delta_s|^2 + \alpha_2|\Delta_d|^2 + \beta_1|\Delta_s|^4 + \beta_2|\Delta_d|^4 \\ &+ \beta_3|\Delta_s|^2|\Delta_d|^2 + \beta_4\left(\Delta_s^{*2}\Delta_d^2 + \Delta_s^2\Delta_d^{*2}\right) + \gamma_1|\boldsymbol{D}\Delta_s|^2 \\ &+ \gamma_2|\boldsymbol{D}\Delta_d|^2 + \gamma_{12}[(D_y\Delta_s)^*(D_y\Delta_d) - (D_x\Delta_s)^*(D_x\Delta_d) \\ &+ \text{c.c.}] + \frac{1}{2}(\boldsymbol{\nabla}\times\tilde{\boldsymbol{A}})^2, \end{aligned} \tag{3}$$

where $D_i = \partial_i + iq\tilde{A}_i$ is a covariant derivative, $\tilde{\boldsymbol{A}} = \sqrt{\frac{L_z}{\mu_0 t_{xy}}}\boldsymbol{A}$, and $q = 2\frac{ea}{\hbar}\sqrt{\frac{\mu_0 t_{xy}}{L_z}}$. The Ginzburg-Landau distance is in units of the unit-cell size a. Note that we expect the Ginzburg-Landau expansion to fail at low temperature. Details of the microscopic derivation of the Ginzburg-Landau coefficients are presented in Appendix B.

A. Coherence length estimates

The resulting Ginzburg-Landau model is (i) anisotropic and (ii) there is an interband potential coupling ($\beta_{3,4}$) and mixed gradient coupling γ_{12}. In general, these types of couplings create a hybridization of normal modes [10,21,22]: that is, a small variation in one of the gap fields causes a small variation in another, and vice versa. Furthermore, in an anisotropic case, the resulting length scales should also depend on the chosen direction, i.e., fields recover their asymptotic form at different direction-dependent scales, away from a local perturbation [23]. Exact evaluation of length scales leads to a degree 6 polynomial equation (for amplitudes, phase difference, and three gauge field components) that determine all the length scales in the system, while all the normal modes are, in general, mixed in the models of the type of Eq. (3) [22]. For our purpose here, it is sufficient to make a rough estimate, that will follow by a numerical analysis: we first neglect the fact that the relative phase θ changes for small amplitude fluctuations and vice versa. This assumption, in fact, breaks for vortex core analysis. However, this method allows us to get a coarse estimate and to illustrate the principle. For a precise description, we will resort to numerical calculations in the next subsection. The magnetic field penetration depth λ and coherence lengths ξ_i are obtained by linearizing the free energy F with respect to variations in the order parameter amplitudes ($|\Delta_{s/d}| = |\Delta_{s/d}^{\text{GS}}| + \sigma_{s/d}$ where $\sigma_{s/d}$ is small) in the direction $\boldsymbol{n} = (\cos\varphi, \sin\varphi)$:

$$\begin{aligned} F_{\text{lin}} &= F_{\text{GS}} + \frac{1}{2}(\boldsymbol{\nabla}_{\boldsymbol{n}}\sigma_\alpha^*)\Gamma_{\alpha\beta}(\boldsymbol{\nabla}_{\boldsymbol{n}}\sigma_\beta) + \frac{1}{2}\sigma_\alpha^*\mathcal{H}_{\alpha\beta}\sigma_\beta \\ &+ q^2|\tilde{\boldsymbol{A}}|^2\left(\gamma_1\left|\Delta_s^{\text{GS}}\right|^2 + \gamma_2\left|\Delta_d^{\text{GS}}\right|^2\right) + \frac{(\boldsymbol{\nabla}\times\tilde{\boldsymbol{A}})^2}{2}. \end{aligned} \tag{4}$$

Here $\mathcal{H}$ is the Hessian matrix of potential energy about the ground state

$$\mathcal{H} = \begin{pmatrix} 8\beta_1|\Delta_s^{\text{GS}}|^2 & 4\tilde{\beta}_3(\theta^{\text{GS}})|\Delta_s^{\text{GS}}||\Delta_d^{\text{GS}}| \\ 4\tilde{\beta}_3(\theta^{\text{GS}})|\Delta_s^{\text{GS}}||\Delta_d^{\text{GS}}| & 8\beta_2|\Delta_d^{\text{GS}}|^2 \end{pmatrix} \tag{5}$$

with $\tilde{\beta}_3(\theta) = \beta_3 + 2\beta_4\cos 2\theta$ and $\theta^{\text{GS}} = \pi/2$. Matrix Γ depends on angle φ between the chosen direction $\boldsymbol{n} = (\cos\varphi, \sin\varphi)$ and the x axis:

$$\Gamma(\varphi) = 2\begin{pmatrix} \gamma_1 & -\gamma_{12}\cos 2\varphi \\ -\gamma_{12}\cos 2\varphi & \gamma_2 \end{pmatrix}. \tag{6}$$

It describes the gradient energy for an amplitude perturbation in the direction $\boldsymbol{n}$. Note that off-diagonal terms describing mixed gradient terms vanish for diagonal propagation directions.

The magnetic field penetration depth λ in SI units can be *roughly estimated* as

$$\lambda^{-1} = 2\frac{e}{\hbar}\sqrt{\frac{\mu_0 t_{xy}}{L_z}}\sqrt{2\left(\gamma_1\left|\Delta_s^{\text{GS}}\right|^2 + \gamma_2\left|\Delta_d^{\text{GS}}\right|^2\right)}. \tag{7}$$

Each amplitude eigenmode has a direction-dependent coherence length ξ_i which, within the approximation, is given by

$$\xi_i(\boldsymbol{n}) = \frac{a}{\sqrt{\eta_i(\varphi)}}, \tag{8}$$

where $\eta_i(\varphi)$ are eigenvalues of $\Gamma^{-1}(\varphi)\mathcal{H}$. In general, the coherence lengths $\xi_i(\boldsymbol{n})$ are associated with linear combinations of σ_s and σ_d, which gives rise to a hybridization of eigenmodes. The presence of off-diagonal terms in $\Gamma(\varphi)$ is crucial: It ensures that the system has two coherence lengths for amplitudes even for a ground state with pure s wave or pure d wave, and suppressed subdominant component.

Within the outlined above approximate approach, a coherence length for relative phase variations ξ_θ is obtained by linearizing the free energy F with respect to phase-difference-only fluctuations ($\theta = \theta^{\text{GS}} + \phi$ where ϕ is small)

$$F_{\text{lin}\phi} = F_{\text{GS}} + \frac{1}{2}K_{\text{rel}}(\varphi, \theta^{\text{GS}})(\boldsymbol{\nabla}\phi)^2 + \frac{1}{2}\left.\frac{\partial^2 F_p}{\partial\theta^2}\right|_{\theta=\theta^{\text{GS}}}\phi^2, \tag{9}$$

where K_{rel} is the relative stiffness and F_p is potential part of the free energy (3). Full expressions are presented in Appendix C 1. Coherence length for relative phase variations

$$\xi_\theta(\varphi) = a\sqrt{\frac{\gamma_1\gamma_2}{\beta_3\left(\gamma_1\left|\Delta_s^{\text{GS}}\right|^2 + \gamma_2\left|\Delta_d^{\text{GS}}\right|^2\right)}} \tag{10}$$

is independent of the direction φ. Note that it is defined in the region with two nucleated gap components ($s + id$ phase in our case) as can be seen in Fig. 2. Let us now compute the length scales in SI units for the unit-cell size $a = 0.4$ nm, interlayer distance $L_z = 1.3$ nm, and hopping parameter $t_{xy} = 0.01$ eV. These are typical values used for the 122-family of iron-based superconductors [24] (as an example). Figure 2 shows the temperature dependence of the coherence lengths and magnetic field penetration depth for fixed chemical potential $\mu = 1.665$ (vertical cross section through red and green points in Fig. 1). The type-1.5 superconductivity regime arises when the magnetic penetration depth λ (black line) is between

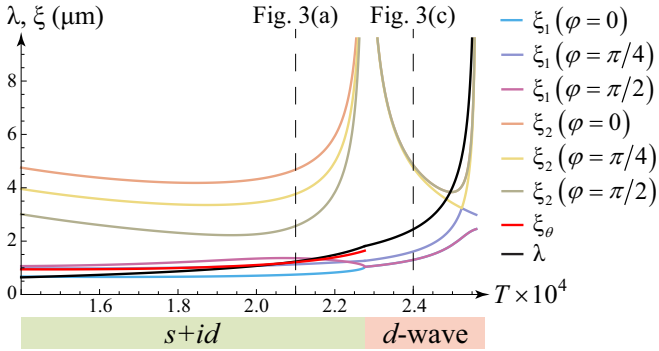


FIG. 2. Temperature dependence of estimates of coherence lengths $\xi_{1(2)}(\varphi)$ for amplitude fluctuation in different directions defined by the angle φ from the x axis, coherence length ξ_θ for phase difference, and magnetic field penetration length λ. Coherence length ξ_θ and magnetic field penetration length λ are independent on the direction in the assumption of no mode mixing. A coherence length for amplitude fluctuation diverges at superconducting phase transition, another divergent length scale occurs at time-reversal symmetry-breaking transition. This divergence occurs at both sides of the phase transitions, even when subdominant order parameter is suppressed. Type-1.5 superconductivity regime arises when magnetic field penetration length is the intermediate length scale, i.e., when λ (black line) is in-between ξ's (colored lines). Chemical potential $\mu = 1.665$, other parameters are identical to Fig. 1.

coherence lengths ξ's (colored lines). Based on this constraint, we can calculate bounds for type-1.5 superconductivity and show these on the phase diagram in Fig. 1. This method serves as an approximation since our calculation of the length scale was approximate. However, it provides an estimate for parameter space regions where exact numerical calculation to be performed (see next subsection). From Figs. 1 and 2, there is an indication that a type-1.5 regime could exist for $s + id$, pure s-wave, and pure d-wave ground states. The latter two cases are the main focus of this paper. One of the coherence lengths ξ diverges at $U(1)$ and $U(1) \to U(1) \times \mathbb{Z}_2$ phase transitions, whereas the magnetic field penetration depth diverges only at the $U(1)$ phase transition. Hence, type-1.5 superconductivity behavior is a generic type of superconductivity of double-transition superconductors. However, there can be purely type-I behavior.

B. Numerical calculations

Since our estimates of coherence lengths relied on analytical approximations, we next study the full Ginzburg-Landau model numerically. In that approach we obtain vortex interaction behavior by performing numerical calculations in a microscopically derived Ginzburg-Landau model. Nontrivial hierarchy of the length scales should manifest itself in numerical simulations as long-range attractive, short-range repulsive intervortex forces.

We pick three points in the phase diagram (Fig. 1) with $s + id$, pure s-wave, and pure d-wave ground states inside the *estimated* type-1.5 regime. The Ginzburg-Landau calculations presented in Fig. 3 show that vortices form clusters. The numerically calculated binding, or interaction, energy is negative for the three phase diagram points (Fig. 4). Hence, the type-1.5 regime is confirmed for all three points, which we estimated to display this hierarchy of the length scales. Note that vortex interaction energy for $s + id$ ground state is one order of magnitude larger than for pure s wave or pure d wave.

The interesting aspect of the vortex clustering in a $s + id$ superconductor is its nontrivial morphology, that can be used to diagnose the symmetry of the pairing state and map phase diagram (for example of experimental morphology analysis see [17]). Two-, three-, and five-vortex clusters form chains along diagonals for a minimal energy state (see Figs. 5 and 6). The stripelike morphology contrasts to circular clusters in multiband s-wave superconductors [25] but it is similar to anisotropic s-wave models [23]. The four-vortex cluster is a diagonal chain for an $s + id$ ground-state parameter set, whereas it forms a diamond for an s-wave ground state. Diamond and chain vortex configurations have identical (up to numerical accuracy) energy for d-wave ground state with four vortices. Hence, the preferred multivortex configurations are very sensitive to the model parameters. On the contrary, $N = 3$, 4 vortex clusters are regular polygons for isotropic multiband models. Note that vortices exhibit type-1.5 behavior along any direction $\boldsymbol{n}$ for the presented parameter sets. However, vortex clusters aligned diagonally relative to crystalline axes have lower interaction energy.

While we focus on length scales' hierarchy and interactions, it is also useful to note that the vortex in Fig. 3(a) (with $s + id$ ground state) carries a nontrivial skyrmionic topological charge, e.g., corresponding to a skyrmion. The topological charge $\mathcal{Q}$ can be computed using the following integral representation (see a detailed discussion in [27]):

$$\mathcal{Q}(\phi) = \frac{i\epsilon_{ji}}{2\pi} \int_{\mathbb{R}^2} \mathrm{d}^2x \, \frac{1}{|\Psi|^4} (|\Psi|^2 \partial_i \Psi^\dagger \partial_j \Psi + \Psi^\dagger \partial_i \Psi \partial_j \Psi^\dagger \Psi), \tag{11}$$

where $\Psi = (\Delta_s, \Delta_d)$. Vortex cores in different components are *spatially separated*, which can be seen from Figs. 3(a1) and 3(a2), and the pseudospin texture of the skyrmion is displayed in Fig. 7. Such vortex core fractionalization can be detected by scanning tunneling microscopy and was recently reported in a different system [28]. The two-vortex state has topological (skyrmion) charge $\mathcal{Q} = 2$ (up to numerical accuracy). For discussion of skyrmions in other regimes and other superconducting models with broken time-reversal symmetry see [27,29,30]. The skyrmion is composed of two $\mathcal{Q} = 1$ skyrmions with relative orientation corresponding to their attraction. Skyrmions are not unique features of type-1.5 superconductivity. However, in the type-1.5 regime there is an additional attractive density-density interaction for skyrmions, giving rise to skyrmion clustering, just as for vortices.

IV. CONCLUSION

In this paper, we studied correlation lengths and vortex physics in a system with s- and d-wave pairing. The particularly interesting aspect, not discussed in previous studies, is the arising of multiple correlation lengths for a state that not only has one broken symmetry, but also a single order parameter, nearly generically leading to the breakdown of

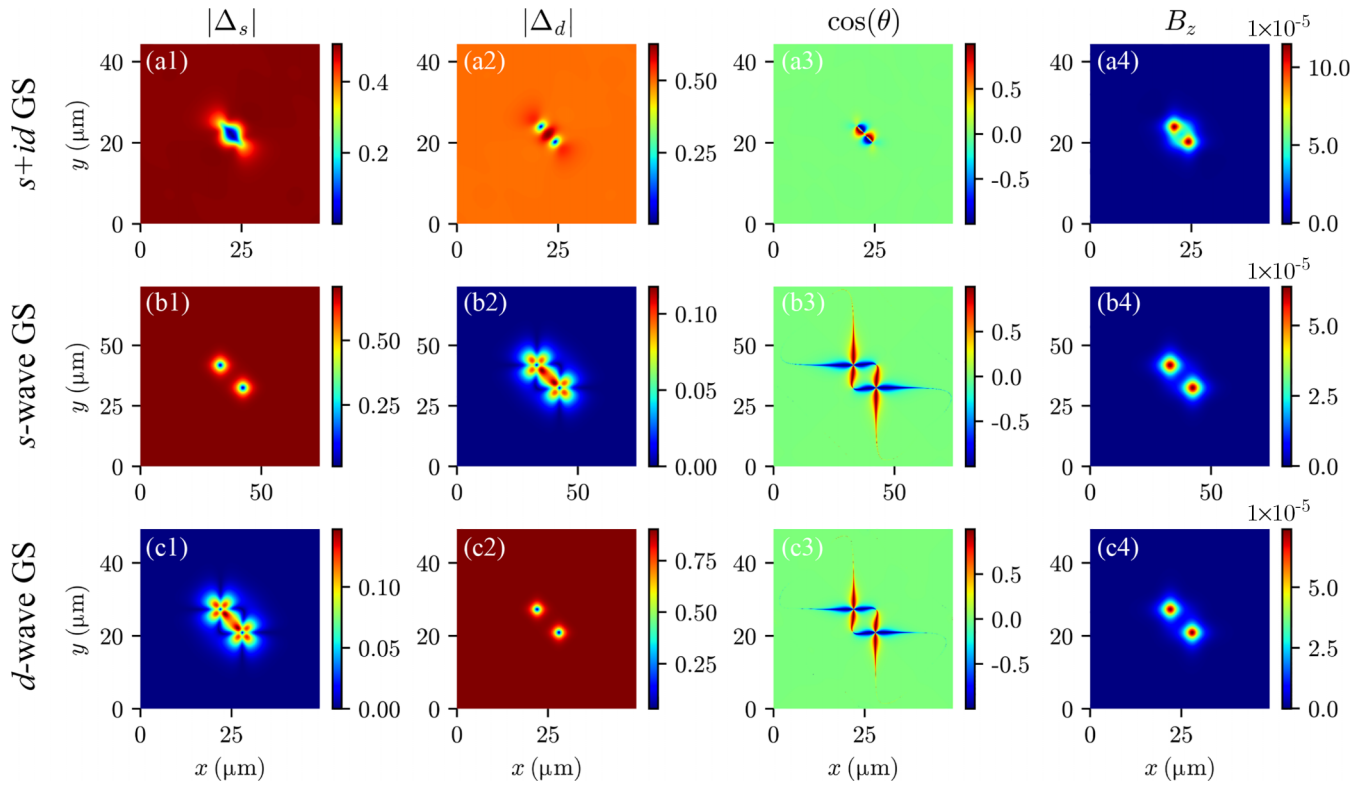


FIG. 3. Two flux quanta vortex cluster solutions in Ginzburg-Landau model for three distinct ground states: (a) $s + id$ state, (b) pure s wave, and (c) pure d wave. The ground states (GSs) correspond to green, black, and red points in Fig. 1. Panels 1–4 show amplitudes $|\Delta_s|$, $|\Delta_d|$, relative phase difference $\theta = \arg(\Delta_s \Delta_d^*)$, and magnetic field B_z. Vortex interaction energy is negative that can be seen in Fig. 4. The total energy density qualitatively follows the magnetic field shown in panel 4. Boundary conditions correspond to no current flowing through the boundary, and the external magnetic field is zero. Gap amplitudes are presented in units $t_{xy}\sqrt{|\alpha_1|/\beta_1}$, magnetic field B_z in $2\hbar|\alpha_1|/(ea^2\gamma_1)$. Model parameters are presented in Table I.

the type-I and type-II dichotomy. Namely, we showed that a competing, although suppressed, order parameter, belonging to a different gap irreducible representation of nonlocal pairing, close to another pairing instability, generically imprints a secondary correlation length on a single condensate and qualitatively alters the magnetic response of a system. The extra length scale arises from the suppressed subdominant order parameter, which only nucleates near the vortex core, but gives a nontrivial hierarchy of the length scales of the problem.

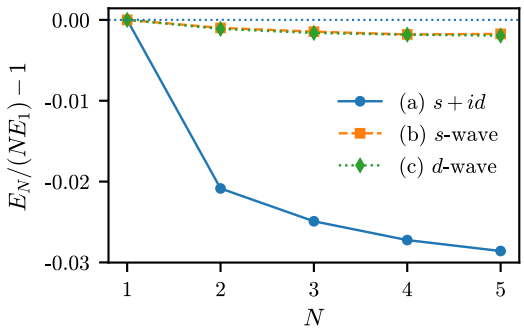


FIG. 4. The normalized binding energy in a vortex cluster per vortex $E_{\text{bind}}/E_1 = E_N/(NE_1) - 1$ shown for the three distinct regimes. Parameter sets correspond to green ($\mu = 1.665$, $T = 2.1 \times 10^{-4}$), black ($\mu = 1.673$, $T = 2.48 \times 10^{-4}$), and red ($\mu = 1.665$, $T = 2.4 \times 10^{-4}$) points in Fig. 1. Ginzburg-Landau model parameters are presented in Table I.

This situation that we discussed should be more generic than our particular microscopic example. Multiple correlation lengths can also arise when the system is parametrically close to any other superconducting instability belonging to a different irreducible representation (e.g., $d + ig$ state). The nontrivial hierarchy of the length scales leads to vortex clustering. We note that inhomogeneous vortex states are common and generic, and in the single-component case are always attributed to pinning, except for extreme proximity to the type-I case where effects beyond Ginzburg-Landau theory become important [31]. Our results call for a more careful look at this experimental data since inhomogeneous vortex distribution can also arise or be enhanced by competing fundamental length scales.

These effects have consequences not only for the basic question of classification of the superconducting state but can also be utilized in applications. It was shown to lead to enhanced pinning properties, which are important for transport applications [32]. More recently, multiscale superconducting states were shown to have unique applications in quantum technology. Instability due to vortex formation is utilized in single-photon detectors. Vortex clustering arising from competing length scales alters the instabilities of the superconducting state and can be utilized in vortex-based

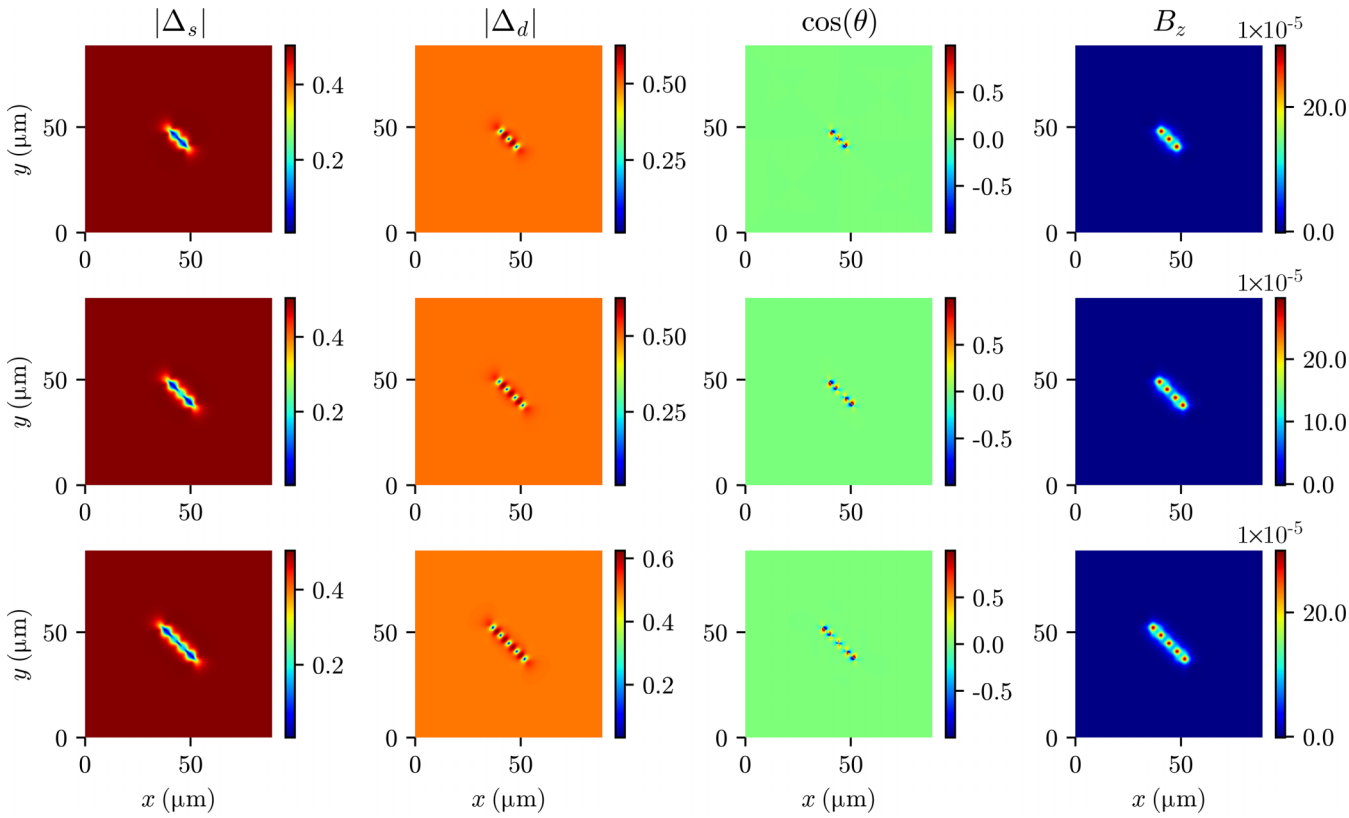


FIG. 5. Vortex cluster solutions for $s + id$ ground state in Ginzburg-Landau model. Number of flux quanta: (a) 3, (b) 4, (c) 5. Model parameters correspond to green point in Fig. 1, it is the first column in Table I. Panels 1–4 show amplitudes $|\Delta_s|$, $|\Delta_d|$, relative phase difference $\theta = \arg(\Delta_s \Delta_d^*)$, and magnetic field B_z. Vortex interaction energy is negative that can be seen in Fig. 4(a). The total energy density qualitatively follows the magnetic field shown in panel 4. Boundary conditions correspond to no current flowing through the boundary, external magnetic field is zero. Gap amplitudes are presented in units $t_{xy}\sqrt{|\alpha_1|/\beta_1}$, magnetic field B_z in $2\hbar|\alpha_1|/(ea^2\gamma_1)$.

superconducting nanowire single-photon detectors. For example, a recent study (Ref. [33]) showed that the type-1.5 hierarchy of the length scales can diminish dark counts in single-photon detectors. Our study shows that one can reach such regimes, favorable for application, e.g., by controlling doping for compounds that have s- and d-wave superconductivity for different compositions.

ACKNOWLEDGMENTS

This work was supported by the Knut and Alice Wallenberg Foundation via the Wallenberg Center for Quantum Technology (WACQT) and by the Swedish Research Council Grant No. 2022-04763. P.L. acknowledges funding from the Olle Engkvists Stiftelse through the Grant No. 226-0103. E.B. was supported by Olle Engkvists Stiftelse a project grant from Knut och Alice Wallenbergs Stiftelse, and partially by the Wallenberg Initiative Materials Science for Sustainability (WISE) funded by the Knut and Alice Wallenberg Foundation.

DATA AVAILABILITY

The data that support the findings of this article are openly available at [34].

APPENDIX A: MICROSCOPIC DESCRIPTION OF PHASE DIAGRAM

The self-consistency equation for superconducting gap has the form

$$\Delta(\boldsymbol{k}) = \frac{1}{N}\sum_{\boldsymbol{k}'} V(\boldsymbol{k},\boldsymbol{k}')\Delta(\boldsymbol{k}')\frac{\tanh\frac{E}{2T}}{2E}, \tag{A1}$$

with only spin-singlet pairing channel

$$\begin{aligned} V(\boldsymbol{k},\boldsymbol{k}') = {} & V(\cos k_x + \cos k_y)(\cos k_x' + \cos k_y') \\ & + V(\cos k_x - \cos k_y)(\cos k_x' - \cos k_y'), \end{aligned} \tag{A2}$$

where N is the number of sites in the lattice, $E = \sqrt{\xi^2 + |\Delta|^2}$ is the quasiparticle excitation energy, ξ is the dispersion relation $[\xi(\boldsymbol{k}) = -2(\cos k_x + \cos k_y) - \mu]$. The sum is computed for energies E smaller than the upper bound denoted ω_D.

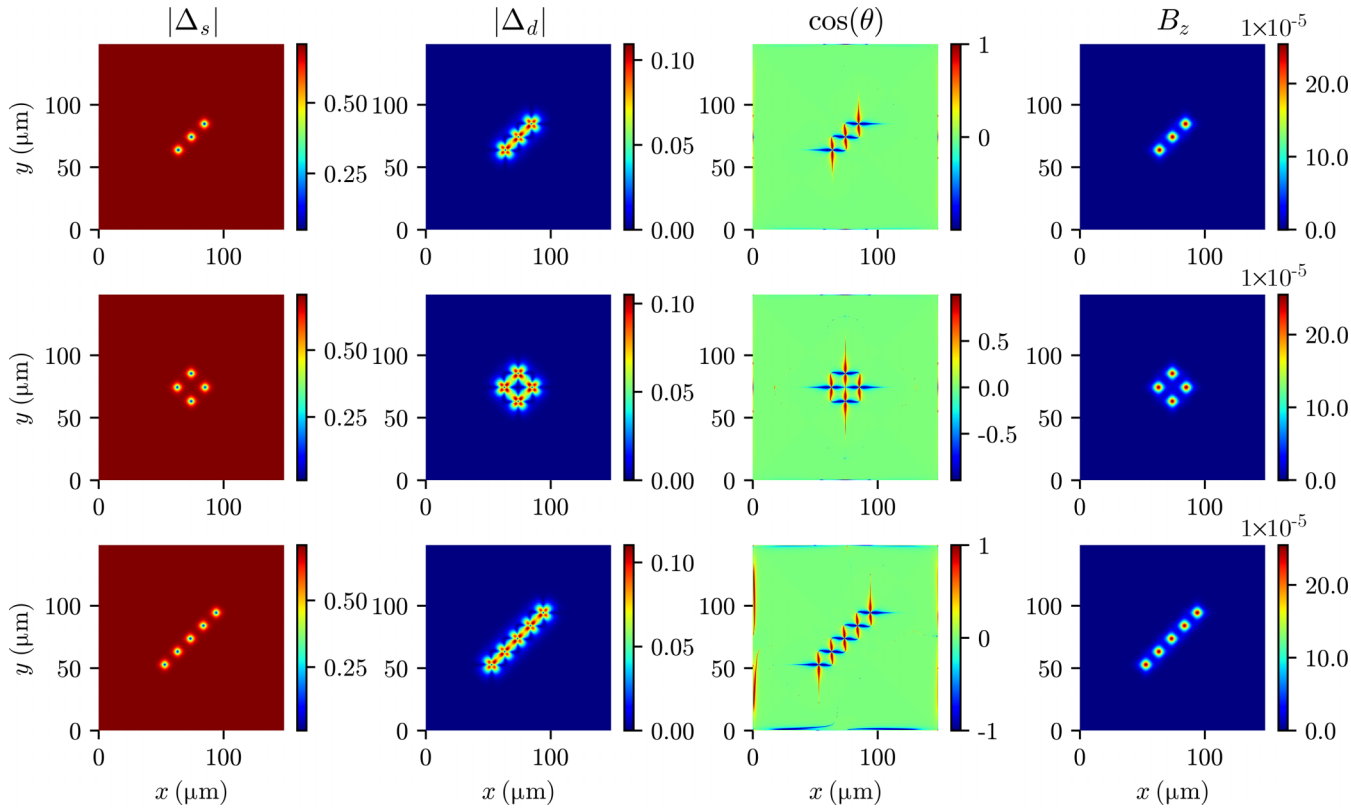


FIG. 6. Vortex cluster solutions for pure s-wave ground state in Ginzburg-Landau model. Number of flux quanta: (a) 3, (b) 4, (c) 5. Model parameters correspond to black point in Fig. 1, it is the second column in Table I. Panels 1–4 show amplitudes $|\Delta_s|$, $|\Delta_d|$, relative phase difference $\theta = \arg(\Delta_s \Delta_d^*)$, and magnetic field B_z. Vortex interaction energy is negative, that can be seen in Fig. 4(b). The total energy density qualitatively follows the magnetic field shown in panel 4. Boundary conditions correspond to no current flowing through the boundary, external magnetic field is zero, and the sample size is chosen so that vortex interaction with boundaries is negligible. Gap amplitudes are presented in units $t_{xy}\sqrt{|\alpha_1|/\beta_1}$, magnetic field B_z in $2\hbar|\alpha_1|/(ea^2\gamma_1)$.

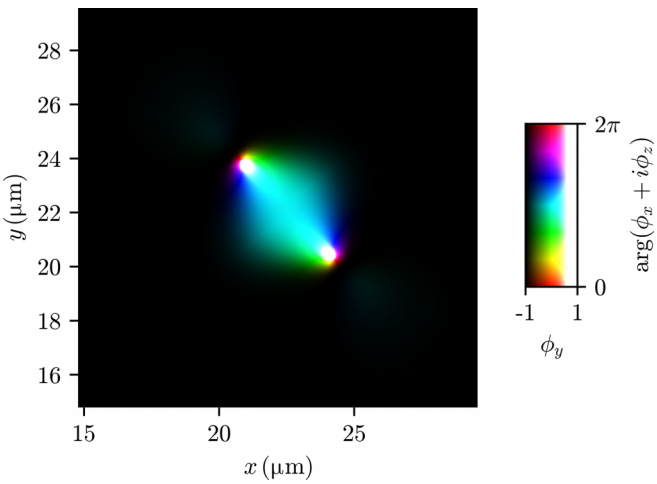


FIG. 7. Plot of the pseudospin texture $\vec{\phi} = \frac{1}{|\Delta_s|^2+|\Delta_d|^2}[\Delta_s^*\Delta_d + \Delta_s\Delta_d^*,\ i(\Delta_s^*\Delta_d - \Delta_s\Delta_d^*),\ |\Delta_d|^2 - |\Delta_s|^2]$ in the $s+id$ regime [Fig. 3(a)]. It shows that the double-quanta vortex is a skyrmion with topological charge $\mathcal{Q} = 2$. In the type-1.5 regime it is a bound state of two $\mathcal{Q} = 1$ skyrmions. The skyrmions are (iso)rotated relative to one another such that the interaction energy between them is minimized. The skyrmion coloring is the standard Runge coloring scheme [26].

Self-consistency (A1) can be separated to the following system:

$$\Delta_s = \Delta_s \frac{1}{N}\sum_{\boldsymbol{k}} V(\cos k_x + \cos k_y)^2 \frac{\tanh\frac{E(\boldsymbol{k})}{2T}}{2E(\boldsymbol{k})},$$
$$\Delta_d = \Delta_d \frac{1}{N}\sum_{\boldsymbol{k}} V(\cos k_x - \cos k_y)^2 \frac{\tanh\frac{E(\boldsymbol{k})}{2T}}{2E(\boldsymbol{k})}. \tag{A3}$$

Here, s and d waves are still implicitly coupled through energy E. The stationary solution of Eq. (A3) is obtained when the sums in the right-hand sides of Eq. (A3) are equal to unity or an order parameter component (Δ_s, Δ_d or both) is 0. For numerical calculations, the sum is presented as an integral over the first Brillouin zone ($\frac{1}{N}\sum_{\boldsymbol{k}} = \int_{\mathrm{BZ}} \frac{d\boldsymbol{k}}{S_{\mathrm{BZ}}}$ taking into account the limits of ω_D). However, for analytical calculations, we use constant density of states [$\rho(\xi,\varphi) \approx N_F$] approximation similar to the Bardeen-Cooper-Schrieffer (BCS) theory [35] [$\frac{1}{N}\sum_{\boldsymbol{k}} = \int_0^{2\pi}\frac{d\varphi}{2\pi}\int_{-\omega_D}^{\omega_D} d\xi\,\rho(\xi,\varphi) \approx 2\int_0^{2\pi}\frac{d\varphi}{2\pi}\int_0^{\omega_D} d\xi N_F$]. Another simplification is that form factors $(\cos k_x \pm \cos k_y)^2$ can be approximated as $\gamma_s \equiv \langle(\cos k_x + \cos k_y)^2\rangle_{\mathrm{FS}}$ for s wave and $\Gamma_d \cos^2 2\varphi$ [$\Gamma_d/2 \equiv \langle(\cos k_x - \cos k_y)^2\rangle_{\mathrm{FS}} = \gamma_d$] for d wave [36,37]. Here $\langle\ldots\rangle_{\mathrm{FS}}$ means the average over the Fermi

surface (FS). Using the above-mentioned assumptions, self-consistency (A3) for $s+id$ state becomes

$$\Delta_s = \Delta_s V N_F \gamma_s \int_0^{2\pi} \frac{d\varphi}{2\pi} \int_0^{\omega_D} d\xi \frac{\tanh \frac{\sqrt{\xi^2+\Delta_s^2+\Delta_d^2\cos^2 2\varphi}}{2T}}{\sqrt{\xi^2+\Delta_s^2+\Delta_d^2\cos^2 2\varphi}},$$

$$\Delta_d = \Delta_d V N_F \Gamma_d \int_0^{2\pi} \frac{d\varphi}{2\pi} \cos^2 2\varphi \int_0^{\omega_D} d\xi \frac{\tanh \frac{\sqrt{\xi^2+\Delta_s^2+\Delta_d^2\cos^2 2\varphi}}{2T}}{\sqrt{\xi^2+\Delta_s^2+\Delta_d^2\cos^2 2\varphi}}. \quad \text{(A4)}$$

Further, the system of equations is analyzed in special cases of low temperature and close to $U(1)$ critical temperature for states corresponding to pure s-wave ($\Delta_d = 0$), pure d -wave ($\Delta_s = 0$), and $s+id$ state. This is done to analytically address the shape of $s+id$ dome in the phase diagram in Fig. 1.

1. Characteristic temperatures for pure s-wave and d-wave $U(1)$ transitions

If s- and d-wave order parameters *would not feel (or influence) each other* [$\Delta_d = 0$ in the first of Eqs. (A4) and $\Delta_s = 0$ in the second equation], *characteristic* temperatures for normal metal to superconductor transition are defined from independent equations

$$V N_F \gamma_s \int_0^{2\pi} \frac{d\varphi}{2\pi} \int_0^{\omega_D} d\xi \frac{\tanh \frac{\xi}{2T_s}}{\xi} = 1, \quad \text{(A5a)}$$

$$V N_F \Gamma_d \int_0^{2\pi} \frac{d\varphi}{2\pi} \cos^2 2\varphi \int_0^{\omega_D} d\xi \frac{\tanh \frac{\xi}{2T_d}}{\xi} = 1. \quad \text{(A5b)}$$

The integral is a standard one with the result $\ln \frac{2e^\gamma \omega_D}{\pi T_c}$, where γ is Euler's constant. So the characteristic temperatures have the form [37]

$$T_s = \frac{2e^\gamma}{\pi} \omega_D \exp\left(-\frac{1}{V N_F \gamma_s}\right), \quad \text{(A6a)}$$

$$T_d = \frac{2e^\gamma}{\pi} \omega_D \exp\left(-\frac{1}{V N_F \Gamma_d/2}\right). \quad \text{(A6b)}$$

Remember that the result holds only for a normal metal to pure s-wave (or pure d-wave) transition. Therefore, only $\max(T_s, T_d)$ determines $U(1)$ symmetry-breaking transition and can be called superconducting critical temperature. However, the concept and notation of the two *characteristic* temperatures that *do not influence each other* will be useful later in the section.

2. Pure s-wave to $s+id$ state transition for all temperatures

Transition from $U(1)$ broken symmetry state to $U(1)\times\mathbb{Z}_2$ state is of the second order in the model at the mean-field level [18,19,38–41]. We can assume $\Delta_s \neq 0$, $\Delta_d \to 0$ for $s+id$ state to s-wave transition. Self-consistency (A4) on the transition line becomes

$$1 = V N_F \gamma_s \int_0^{\omega_D} d\xi \frac{\tanh \frac{\sqrt{\xi^2+\Delta_s^2}}{2T}}{\sqrt{\xi^2+\Delta_s^2}},$$

$$1 = V N_F \gamma_d \int_0^{\omega_D} d\xi \frac{\tanh \frac{\sqrt{\xi^2+\Delta_s^2}}{2T}}{\sqrt{\xi^2+\Delta_s^2}}. \quad \text{(A7)}$$

If the first equation is satisfied, we know Δ_s for given T, μ. The second equation is satisfied when $\gamma_d = \gamma_s$ ($\gamma_d = \Gamma_d/2$) in the BCS limit. This coincides with the conclusion of Ref. [19] which deals only with $T = 0$ case. The form factor $\gamma = \langle(\cos k_x + \cos k_y)^2\rangle_{\mathrm{FS}}$ depends only on the chemical potential μ. Hence, the transition line does not depend on the temperature (assuming $T < T_s$). Therefore, the transition is a vertical line ($\mu = \mathrm{const}$) on the (μ, T) phase diagram (see numerical calculation results in Figs. 1, 8, and Refs. [18,42]). A phase diagram with a sharp boundary between s-wave phase and nematic phase with broken time-reversal symmetry was discussed in connection of iron-based superconductors (see, e.g., [43]).

Note that, experimentally, one investigates electron density n-temperature T phase diagram because the number of electrons in the sample is fixed during the measurement. The relation between electron density and chemical potential is the following:

$$n = \frac{1}{N} \sum_{\boldsymbol{k}} \left[1 - \frac{\xi}{E} \tanh\left(\frac{E}{2T}\right)\right], \quad \text{(A8)}$$

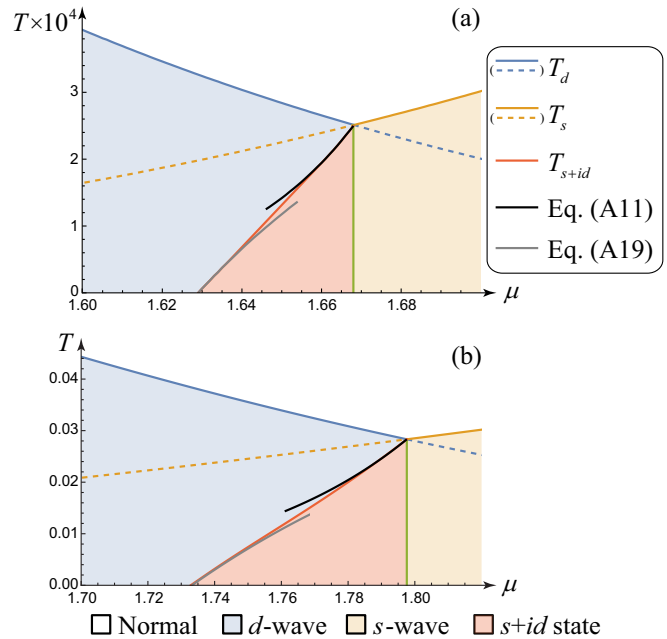


FIG. 8. The phase diagram of the microscopic Hamiltonian (1) in chemical potential μ, temperature T coordinates. (a) Energy cutoff $\omega_D = 0.1$, (b) $\omega_D \to \infty$ (full Brillouin zone contributes). Orange and blue dashed lines for T_s and T_d do not correspond to phase transitions. Nearest-neighbor interaction strength V is 2.

where ξ depends on μ and E depends on μ and T [through $\Delta(T)$], $n \in [0;2]$. This electron density is a measure of the asymmetry between the positive and negative excitations of ξ. However, the change of electron density for $0 \leqslant T \leqslant T_c$ is quite small. Numerically, the change is of the order of 10^{-3} for $|n(\mu, T=0) - n(\mu, T_c)|$ (which is much smaller than typical values of n). Hence, (n, T) phase diagram will look qualitatively similar to (μ, T) phase diagram (see Refs. [44,45]).

3. Pure d-wave to $s+id$ state transition for $(T_d - T) \ll T_d$

In the subsection, we are interested in a region where d wave just developed ($\Delta_d \to 0$), and we are approaching $s+id$ state from d-wave phase ($\Delta_s = 0$). The characteristic temperature for s wave is lower than for d wave in the phase diagram region. Superconducting gap for d wave can be approximately written in the way [19,37]

$$\Delta_d(T) = 4\pi\sqrt{\frac{2}{21\zeta(3)}}T\sqrt{-\ln\frac{T}{T_d}} \approx 3.537T_d\sqrt{1-\frac{T}{T_d}}, \tag{A9}$$

where ζ is the Riemann zeta function. It follows from the second of Eq. (A4).

The first of Eq. (A4) can be simplified in a similar manner to Ref. [37] that derives Eq. (A9). First, Taylor expand integrand up to the second order in Δ_d. Then integrate over ξ using $\int_0^\infty dx(\frac{\tanh x}{x^3} - \frac{1}{x^2}\cosh^2 x) = 7\zeta(3)/\pi^2$ (assuming $\omega_d \gg \Delta_d$) and substitute Eq. (A6a):

$$\begin{aligned}
1 &= VN_F\gamma_s\int_0^{2\pi}\frac{d\varphi}{2\pi}\int_0^{\omega_D}d\xi\frac{\tanh\frac{\sqrt{\xi^2+\Delta_d^2\cos^2 2\varphi}}{2T}}{\sqrt{\xi^2+\Delta_d^2\cos^2 2\varphi}} \\
&\approx VN_F\gamma_s\int_0^{2\pi}\frac{d\varphi}{2\pi}\left[\int_0^{\omega_D}d\xi\frac{\tanh\frac{\xi}{2T}}{\xi}\right. \\
&\quad \left. -\int_0^{\omega_D}d\xi\left(\frac{\tanh\frac{\xi}{2T}}{2\xi^3} - \frac{1-\tanh^2\frac{\xi}{2T}}{4T\xi^2}\right)\Delta_d^2\cos^2 2\varphi\right] \\
&= VN_F\gamma_s\left[\ln\frac{T_s}{T} - \frac{7\zeta(3)}{16T^2\pi^2}\Delta_d^2(T)\right] + 1.
\end{aligned} \tag{A10}$$

This equation only holds at the transition between pure d wave to $s+id$ state. Combining Eqs. (A9) and (A10) one gets

$$T_{d\text{ to }s+id} = \frac{T_s^3}{T_d^2} = \frac{2e^\gamma\omega_D}{\pi}\exp\left[-\frac{1}{VN_F}\left(\frac{3}{\gamma_s} - \frac{2}{\Gamma_d/2}\right)\right]. \tag{A11}$$

This equation also defines a point where all four phases coexist ($T = T_s = T_d = T_{d\text{ to }s+id}$, $\gamma_s = \gamma_d = \Gamma_d/2$). At this point, the superconducting gap in both channels tends to zero. A similar tetracritical point attracted recent interest [46]. The transition temperature [$T_{d\text{ to }s+id} = T_s^3 T_d^{-2}$] coincides with the result from an analysis of corresponding Ginzburg-Landau (GL) equations [18].

4. Pure d-wave to $s+id$ state transition for $T \ll T_d, T_s$

Self-consistency (A4) becomes

$$\begin{aligned}
1 &= VN_F\gamma_s\int_0^{2\pi}\frac{d\varphi}{2\pi}\int_0^{\omega_D}d\xi\frac{\tanh\frac{\sqrt{\xi^2+\Delta_d^2\cos^2 2\varphi}}{2T}}{\sqrt{\xi^2+\Delta_d^2\cos^2 2\varphi}}, \\
1 &= VN_F\Gamma_d\int_0^{2\pi}\frac{d\varphi}{2\pi}\cos^2 2\varphi\int_0^{\omega_D}d\xi\frac{\tanh\frac{\sqrt{\xi^2+\Delta_d^2\cos^2 2\varphi}}{2T}}{\sqrt{\xi^2+\Delta_d^2\cos^2 2\varphi}}.
\end{aligned} \tag{A12}$$

Let us work with the first equation of Eq. (A12). Add and subtract term $\frac{1}{\sqrt{\xi^2+\Delta_d^2\cos^2 2\varphi}}$ to the integral:

$$\begin{aligned}
\frac{1}{VN_F\gamma_s} &= \int_0^{2\pi}\frac{d\varphi}{2\pi}\int_0^{\omega_D}d\xi\left(\frac{\tanh\frac{\sqrt{\xi^2+\Delta_d^2\cos^2 2\varphi}}{2T}}{\sqrt{\xi^2+\Delta_d^2\cos^2 2\varphi}} - \frac{1}{\sqrt{\xi^2+\Delta_d^2\cos^2 2\varphi}} + \frac{1}{\sqrt{\xi^2+\Delta_d^2\cos^2 2\varphi}}\right) \\
&= \int_0^{2\pi}\frac{d\varphi}{2\pi}\int_0^{\omega_D}\frac{d\xi}{\sqrt{\xi^2+\Delta_d^2\cos^2 2\varphi}}\left(\tanh\frac{\sqrt{\xi^2+\Delta_d^2\cos^2 2\varphi}}{2T} - 1\right) + \ln\frac{4\omega_D}{\Delta_d},
\end{aligned} \tag{A13}$$

where the second integral $\int_0^{2\pi}\frac{d\varphi}{2\pi}\int_0^{\omega_D}\frac{d\xi}{\sqrt{\xi^2+\Delta_d^2\cos^2 2\varphi}} = \int_0^{2\pi}\frac{d\varphi}{2\pi}\ln\frac{2\omega_D}{\Delta_d|\cos 2\varphi|} = \ln\frac{4\omega_D}{\Delta_d}$ is computed in the limit $\omega_D \gg \Delta_d(0)$ [37]. In the first integral, we change coordinates to $x = \beta\xi$ ($\beta = T^{-1}$) and $y = \beta\Delta_d\cos 2\varphi$:

$$\frac{1}{VN_F\gamma_s} = \ln\frac{4\omega_D}{\Delta_d} + \frac{1}{2\pi}8\int_0^{\beta\Delta_d}\frac{dy}{2\sqrt{\beta^2\Delta_d^2-y^2}}\int_0^{\beta\omega_D}\frac{dx}{\sqrt{x^2+y^2}}\left(\tanh\frac{\sqrt{x^2+y^2}}{2} - 1\right). \tag{A14}$$

The main contribution to the integral comes from the region where x and y are the smallest. Therefore, we can use approximation $\sqrt{\beta^2\Delta_d^2 - y^2} \approx \beta\Delta_d$:

$$\frac{1}{VN_F\gamma_s} = \ln\frac{4\omega_D}{\Delta_d} + \frac{2T}{\pi\Delta_d}\int_0^{\beta\Delta_d} dy \times \int_0^{\beta\omega_D} \frac{dx}{\sqrt{x^2+y^2}}\left(\tanh\frac{\sqrt{x^2+y^2}}{2} - 1\right). \quad \text{(A15)}$$

The upper bounds for both integrals can be approximated as infinite because $\beta \to \infty$ and Δ_d, ω_D are some not infinitesimal parameters. The integral can be computed in the following way:

$$\int_0^\infty dy \int_0^\infty \frac{dx}{\sqrt{x^2+y^2}}\left(\tanh\frac{\sqrt{x^2+y^2}}{2} - 1\right) = \int_0^{\pi/2} d\varphi \int_0^\infty dr\left(\tanh\frac{r}{2} - 1\right) = -\pi\ln 2. \quad \text{(A16)}$$

Let us substitute this result to Eq. (A15) and substitute Eq. (A6a) to the left-hand side:

$$\ln\frac{2e^\gamma\omega_D}{\pi T_s} = \ln\frac{4\omega_D}{\Delta_d} - \frac{2T\ln 2}{\Delta_d}. \quad \text{(A17)}$$

Therefore, temperature for the pure d wave to $s+id$ state transition is

$$T_{d\text{tos}+id} = \frac{\Delta_d}{2\ln 2}\ln\frac{2\pi T_s}{\Delta_d e^\gamma}. \quad \text{(A18)}$$

The last step is to substitute the superconducting gap at zero temperature [$\Delta_d(0) = 2\pi e^{-\gamma-1/2}T_d$ [19,37]] instead of Δ_d:

$$T_{d\text{ to }s+id} = \frac{\pi e^{-\gamma-1/2}T_d}{\ln 2}\ln\frac{T_s e^{1/2}}{T_d} = \frac{2\omega_D}{\sqrt{e}\ln 2}\left(\frac{1}{2} + \frac{1}{VN_F\Gamma_d/2} - \frac{1}{VN_F\gamma_s}\right)e^{-2/VN_F\Gamma_d}. \quad \text{(A19)}$$

For zero temperature of the transition, we have

$$\frac{1}{2} = \frac{1}{VN_F}\left(\frac{1}{\gamma_s} - \frac{2}{\Gamma_d}\right) = \ln\frac{T_d}{T_s}. \quad \text{(A20)}$$

So the transition happens when $T_d = T_s e^{1/2}$ if one uses auxiliary characteristic temperature for s wave (which does not correspond to a phase transition). The left part of Eq. (A20) was also obtained in Ref. [19].

5. Numerical calculations of a phase diagram and comparison to analytical results

Let us compute superconducting phase diagram in (μ, T) coordinates using numerical solution of Eq. (A3) with a small energy cutoff [$\omega_D = 0.1$, see Fig. 8(a)]. A distinct feature is a sharp (vertical) transition between $s+id$ and s-wave phases, predicted in Appendix A 2. Numerically, we see that $\mu_{s\text{ to }s+id}$ varies, but the chemical potential change between $T=0$ and $T = T_s = T_d$ is $O(10^{-5})$ and close to the computational precision. High- and low-temperature approximations [Eqs. (A11) and (A19), respectively] describe d wave to $s+id$ state transition quite well. They hold far beyond the temperature range assumptions made for their derivation.

As a limiting type of check, we use the assumption of no energy cutoff (for a square lattice $\omega_D > 8$ has the same properties). This means that all excitations from the dispersion relation [$\xi(\boldsymbol{k}) = -2(\cos k_x + \cos k_y) - \mu$] contribute to the Cooper pairing [in Eq. (A3) all momenta are considered]. The numerically obtained phase diagram in coordinates (μ, T) is presented in Fig. 8(b). High- and low-temperature approximations [Eqs. (A11) and (A19), respectively] are plotted in black and gray colors. They are in good agreement with numerical results even beyond the validity of the approximations. Namely, Eq. (A19) works for $T < 0.2T_d$ ($T < 0.3T_s$) compared to initial constraint $T \ll T_d, T_s$. And Eq. (A11) works for $T > 0.8T_d$ compared to $(T_d - T) \ll T_d$. Recall that analytical results were derived within the BCS approximation ($T \ll \omega_D \ll 1$). However, as we can see, the results can also be applied to large quasiparticle energy excitations using effective values of superconducting form factors.

APPENDIX B: DERIVATION OF GINZBURG-LANDAU EQUATIONS FROM MICROSCOPIC MODEL

The derivation of GL equations is based on expanding Gor'kov's (microscopic self-consistency) equations in powers of order parameter [5]. Below we present a short version. First, we derive potential terms and then kinetic (gradient) terms. We start with introducing notations $f_s(\boldsymbol{k}) = \cos k_x + \cos k_y$, $f_d(\boldsymbol{k}) = \cos k_x - \cos k_y$. Microscopic self-consistency equation (A1) takes the form

$$\begin{aligned}\Delta(\boldsymbol{k}) &= \frac{1}{N}\sum_{\boldsymbol{k}'} V[f_s(\boldsymbol{k})f_s(\boldsymbol{k}') + f_d(\boldsymbol{k})f_d(\boldsymbol{k}')]\Delta(\boldsymbol{k}') \\ &\quad\cdot T\sum_{\omega_n}\frac{1}{\omega_n^2 + \xi^2(\boldsymbol{k}') + |\Delta(\boldsymbol{k}')|^2} \\ &\approx \frac{VT}{N}\sum_{\boldsymbol{k}'}[f_s(\boldsymbol{k})f_s(\boldsymbol{k}') + f_d(\boldsymbol{k})f_d(\boldsymbol{k}')] \\ &\quad\cdot\sum_{\omega_n}\left[\frac{\Delta(\boldsymbol{k}')}{\omega_n^2 + \xi^2(\boldsymbol{k}')} - \frac{\Delta(\boldsymbol{k}')|\Delta(\boldsymbol{k}')|^2}{[\omega_n^2 + \xi^2(\boldsymbol{k}')]^2}\right],\end{aligned} \quad \text{(B1)}$$

where we used identity $T\sum_{\omega_n}(\omega_n^2 + E^2)^{-1} = \frac{\tanh(E/2T)}{2E}$, $\omega_n = (1+2n)\pi T$ are Matsubara frequencies. Next, equations for s- and d-wave components of the order parameter $\Delta(\boldsymbol{k}) = \Delta_s f_s(\boldsymbol{k}) + \Delta_d f_d(\boldsymbol{k})$ can be separated:

$$\begin{aligned}&\Delta_s\left(\frac{1}{V} - \frac{T}{N}\sum_{\boldsymbol{k}',\omega_n}\frac{f_s^2(\boldsymbol{k}')}{\omega_n^2 + \xi^2(\boldsymbol{k}')}\right) - \Delta_d\frac{T}{N}\sum_{\boldsymbol{k}',\omega_n}\frac{f_s(\boldsymbol{k}')f_d(\boldsymbol{k}')}{\omega_n^2 + \xi^2(\boldsymbol{k}')} + \frac{T}{N}\sum_{\boldsymbol{k}',\omega_n}\frac{1}{\left[\omega_n^2 + \xi^2(\boldsymbol{k}')\right]^2} \\ &\cdot\left[f_s^4(\boldsymbol{k}')|\Delta_s|^2\Delta_s + 2f_d^2(\boldsymbol{k}')f_s^2(\boldsymbol{k}')|\Delta_d|^2\Delta_s + f_d^2(\boldsymbol{k}')f_s^2(\boldsymbol{k}')\Delta_d^2\Delta_s^* \right. \\ &\left. + f_d^3(\boldsymbol{k}')f_s(\boldsymbol{k}')|\Delta_d|^2\Delta_d + f_d(\boldsymbol{k}')f_s^3(\boldsymbol{k}')\left(2|\Delta_s|^2\Delta_d + \Delta_s^2\Delta_d^*\right)\right] = 0.\end{aligned} \quad \text{(B2)}$$

The equation for Δ_d can be obtained by changing indices $s \leftrightarrow d$. The sum over $\boldsymbol{k}'$ is zero for odd in $f_{s/d}$ terms for the tetragonal system because they are odd with respect to $\pi/2$ rotation. Comparing terms from Eq. (B2) and GL equations that follow from Eq. (3) one finds

$$\alpha_1 = \frac{1}{V} - \frac{T}{N}\sum_{\boldsymbol{k},\omega_n} \frac{f_s^2(\boldsymbol{k})}{\omega_n^2 + \xi^2(\boldsymbol{k})},$$

$$\alpha_2 = \frac{1}{V} - \frac{T}{N}\sum_{\boldsymbol{k},\omega_n} \frac{f_d^2(\boldsymbol{k})}{\omega_n^2 + \xi^2(\boldsymbol{k})},$$

$$\{\beta_1, \beta_2, \beta_3, \beta_4\} = \frac{T}{2N}\sum_{\boldsymbol{k},\omega_n} \frac{\left\{f_s^4(\boldsymbol{k}), f_d^4(\boldsymbol{k}), 4f_s^2(\boldsymbol{k})f_d^2(\boldsymbol{k}), f_s^2(\boldsymbol{k})f_d^2(\boldsymbol{k})\right\}}{\left[\omega_n^2 + \xi^2(\boldsymbol{k})\right]^2}. \tag{B3}$$

Note, that $\beta_4 = \beta_3/4$.

Coefficients β_{1-4} differ by factor 4 from corresponding coefficients in Refs. [47,48]. Origin of the difference roots in the gap definition: they use $\Delta(\boldsymbol{k}) = \Delta_s \frac{f_s(\boldsymbol{k})}{2} + \Delta_d \frac{f_d(\boldsymbol{k})}{2}$. Therefore, if quadratic in Δ's terms coincide (situation that we have), quartic terms coefficients should be multiplied by factor of 2^2 when transforming from $\Delta(\boldsymbol{k}) = \Delta_s f_s(\boldsymbol{k}) + \Delta_d f_d(\boldsymbol{k})$ to $\Delta(\boldsymbol{k}) = \Delta_s \frac{f_s(\boldsymbol{k})}{2} + \Delta_d \frac{f_d(\boldsymbol{k})}{2}$.

Now, let us compute gradient terms. Below we derive coefficients only for quadratic in gaps $\Delta_{s/d}$ terms. Self-consistency equation can be written in real space using Green functions $\mathcal{G}_0$ in the absence of a magnetic field ($\boldsymbol{A} = 0$):

$$\frac{1}{V}\Delta_\eta^*(\boldsymbol{r}) = T\sum_{\boldsymbol{r}',\epsilon,\omega_n} \mathcal{G}_0(\boldsymbol{r}', \boldsymbol{r}+\eta, -\omega_n)\Delta_\epsilon^*(\boldsymbol{r}')\mathcal{G}_0(\boldsymbol{r}'+\epsilon, \boldsymbol{r}, \omega_n), \tag{B4}$$

where $\eta, \epsilon = \pm\hat{x}, \pm\hat{y}$, and Green function is assumed to be translationally invariant $\mathcal{G}_0(\boldsymbol{r}', \boldsymbol{r}, \omega_n) = \mathcal{G}_0(\boldsymbol{r}' - \boldsymbol{r}, \omega_n) = \frac{1}{N}\sum_{\boldsymbol{k}} e^{i\boldsymbol{k}(\boldsymbol{r}'-\boldsymbol{r})}/(i\omega_n - \xi_{\boldsymbol{k}})$. Superconducting gap that lives on a links can be expanded in powers of derivatives:

$$\Delta_\epsilon(\boldsymbol{r}') = \Delta_\epsilon(\boldsymbol{r}) + (\boldsymbol{r}'-\boldsymbol{r})_\mu \nabla_\mu \Delta_\epsilon(\boldsymbol{r}) + \frac{1}{2}(\boldsymbol{r}'-\boldsymbol{r})_\mu(\boldsymbol{r}'-\boldsymbol{r})_\nu \nabla_\mu\nabla_\nu \Delta_\epsilon(\boldsymbol{r}). \tag{B5}$$

Here assumed summation over repeated indices. Substituting Green functions and Eq. (B5) to (B4) one gets

$$\frac{1}{V}\Delta_\eta^*(\boldsymbol{r}) = \frac{T}{N^2}\sum_{\boldsymbol{k}_1,\boldsymbol{k}_2,\epsilon,\omega_n} \frac{1}{-i\omega_n - \xi_{\boldsymbol{k}_1}}\frac{1}{i\omega_n - \xi_{\boldsymbol{k}_2}} \Bigg[\Delta_\epsilon^*(\boldsymbol{r}) \underbrace{\sum_{\boldsymbol{r}'} e^{i(\boldsymbol{k}_1+\boldsymbol{k}_2)(\boldsymbol{r}'-\boldsymbol{r})}}_{N\delta_{\boldsymbol{k}_1,\boldsymbol{k}_2}} e^{-i\boldsymbol{k}_1\eta + i\boldsymbol{k}_2\epsilon}$$
$$+\nabla_\mu\Delta_\epsilon^*(\boldsymbol{r}) \sum_{\boldsymbol{r}'} \underbrace{(\boldsymbol{r}'-\boldsymbol{r})_\mu}_{(-i\frac{\partial}{\partial k_{1\mu}} + \eta_\mu)} e^{i(\boldsymbol{k}_1+\boldsymbol{k}_2)(\boldsymbol{r}'-\boldsymbol{r}) - i\boldsymbol{k}_1\eta + i\boldsymbol{k}_2\epsilon} + \frac{1}{2}\nabla_\mu\nabla_\nu\Delta_\epsilon^*(\boldsymbol{r}) \sum_{\boldsymbol{r}'} \underbrace{(\boldsymbol{r}'-\boldsymbol{r})_\mu}_{(-i\frac{\partial}{\partial k_{1\mu}} + \eta_\mu)} \underbrace{(\boldsymbol{r}'-\boldsymbol{r})_\nu}_{(-i\frac{\partial}{\partial k_{2\nu}} - \epsilon_\nu)} e^{i(\boldsymbol{k}_1+\boldsymbol{k}_2)(\boldsymbol{r}'-\boldsymbol{r}) - i\boldsymbol{k}_1\eta + i\boldsymbol{k}_2\epsilon} \Bigg]. \tag{B6}$$

Next, we "integrate by parts" terms containing $\frac{\partial}{\partial k_{1\mu}}$ and $\frac{\partial}{\partial k_{2\nu}}$ and then perform sum over $\boldsymbol{r}'$ like in the first line of Eq. (B6)

$$\frac{1}{V}\Delta_\eta^*(\boldsymbol{r}) = \frac{T}{N}\sum_{\boldsymbol{k},\epsilon,\omega_n} \frac{1}{\omega_n^2 + \xi_{\boldsymbol{k}}^2}\Bigg[\Delta_\epsilon^*(\boldsymbol{r}) + \eta_\mu\nabla_\mu\Delta_\epsilon^*(\boldsymbol{r}) - \frac{1}{2}\eta_\mu\epsilon_\nu\nabla_\mu\nabla_\nu\Delta_\epsilon^*(\boldsymbol{r}) + i\nabla_\mu\Delta_\epsilon^*(\boldsymbol{r})\frac{\partial\xi_{\boldsymbol{k}}/\partial k_\mu}{-i\omega_n - \xi_{\boldsymbol{k}}}$$
$$-\frac{i}{2}\eta_\mu\nabla_\mu\nabla_\nu\Delta_\epsilon^*(\boldsymbol{r})\frac{\partial\xi_{\boldsymbol{k}}/\partial k_\nu}{i\omega_n - \xi_{\boldsymbol{k}}} - \frac{i}{2}\epsilon_\nu\nabla_\mu\nabla_\nu\Delta_\epsilon^*(\boldsymbol{r})\frac{\partial\xi_{\boldsymbol{k}}/\partial k_\mu}{-i\omega_n - \xi_{\boldsymbol{k}}} + \frac{1}{2}\nabla_\mu\nabla_\nu\Delta_\epsilon^*(\boldsymbol{r})\frac{(\partial\xi_{\boldsymbol{k}}/\partial k_\mu)(\partial\xi_{\boldsymbol{k}}/\partial k_\nu)}{\omega_n^2 + \xi_{\boldsymbol{k}}^2}\Bigg]e^{-i\boldsymbol{k}(\eta+\epsilon)}. \tag{B7}$$

All the terms except the first and the last vanish during summation over ϵ and $\boldsymbol{k}$ because they are odd with respect to space inversion (containing ϵ, η) or $\pi/2$ rotation (with $\partial\xi_{\boldsymbol{k}}/\partial k_\mu$). The last term is nonzero only for $\mu = \nu$ for the same reason. These facts significantly simplify self-consistency equation (written up to linear order)

$$\frac{1}{V}\Delta_\eta^*(\boldsymbol{r}) = \frac{T}{N}\sum_{\boldsymbol{k},\epsilon,\omega_n} \frac{1}{\omega_n^2 + \xi_{\boldsymbol{k}}^2}\left[\Delta_\epsilon^*(\boldsymbol{r}) + \frac{1}{2}\frac{\partial^2}{\partial\boldsymbol{r}_\mu^2}\Delta_\epsilon^*(\boldsymbol{r})\frac{(\partial\xi_{\boldsymbol{k}}/\partial k_\mu)^2}{\omega_n^2 + \xi_{\boldsymbol{k}}^2}\right]e^{-i\boldsymbol{k}(\eta+\epsilon)}. \tag{B8}$$

The final step is to introduce extended s- and d-wave order parameters [$\Delta_s = \frac{1}{2}(\Delta_{+\hat{x}} + \Delta_{-\hat{x}} + \Delta_{+\hat{y}} + \Delta_{-\hat{y}})$, $\Delta_d = \frac{1}{2}(\Delta_{+\hat{x}} + \Delta_{-\hat{x}} - \Delta_{+\hat{y}} - \Delta_{-\hat{y}})$], write self-consistency (B8) for these irreducible representations, and compute sum over ϵ:

$$\Delta_s^*\left(\frac{1}{V} - \frac{T}{N}\sum_{\boldsymbol{k},\omega_n}\frac{f_s^2(\boldsymbol{k})}{\omega_n^2 + \xi^2(\boldsymbol{k})}\right) - 2\frac{T}{N}\sum_{\boldsymbol{k},\omega_n}\frac{f_s(\boldsymbol{k})\left[\sin^2(k_x)\frac{\partial^2}{\partial x^2} + \sin^2(k_y)\frac{\partial^2}{\partial y^2}\right]}{\left[\omega_n^2 + \xi^2(\boldsymbol{k})\right]^2}\cdot\left[\Delta_s^* f_s(\boldsymbol{k}) + \Delta_d^* f_d(\boldsymbol{k})\right] = 0. \tag{B9}$$

Here we kept only terms that do not vanish after summation over $\boldsymbol{k}$. Comparing this equation to linearized GL equations from Eq. (3), gradient coefficients take the form

$$\{\gamma_1, \gamma_2, \gamma_{12}\} = 2\frac{T}{N}\sum_{\boldsymbol{k},\omega_n} \sin^2(k_x) \frac{\{f_s^2(\boldsymbol{k}), f_d^2(\boldsymbol{k}), -f_s(\boldsymbol{k})f_d(\boldsymbol{k})\}}{\left[\omega_n^2 + \xi^2(\boldsymbol{k})\right]^2}, \quad \text{(B10)}$$

where γ_2 is derived by analogy.

Inclusion of gauge field $\boldsymbol{A}$ changes derivative ∂_i to covariant one $D_i = \partial_i + i\frac{2ea}{\hbar}A_i$, where factor of 2 emerges due to two electron coupling in the gap Δ.

The free-energy density (3) is defined up to a multiplication factor which can be found by comparison of energies in GL model and microscopic model at $T = 0$. In the Bardeen-Cooper-Schrieffer (BCS) limit it is density of states on the Fermi level.

In the BCS limit ($T \ll \omega_D \ll 1$) GL coefficients can be simplified

$$\alpha_1 \approx \frac{1}{V} - 2\left\langle N_F f_s^2(\boldsymbol{k})\right\rangle_{\text{FS}} \int_0^{\omega_D} d\xi \frac{\tanh\frac{\xi}{2T}}{2\xi} \approx \left\langle N_F f_s^2(\boldsymbol{k})\right\rangle_{\text{FS}} \ln\frac{T}{T_s}, \quad \text{(B11)}$$

where T_s is defined in Eq. (A6a). Similarly $\alpha_2 \approx \langle N_F f_d^2(\boldsymbol{k})\rangle_{\text{FS}} \ln\frac{T}{T_d}$. Coefficients β_{1-4} and γ's have similar structure and can be simplified in the following way:

$$\beta_1 \approx \left\langle N_F f_s^4(\boldsymbol{k})\right\rangle_{\text{FS}} \int_0^{\omega_D} \frac{d\xi}{2\xi^2}\left(\frac{\tanh\frac{\xi}{2T}}{2\xi} - \frac{1}{4T\cosh^2\frac{\xi}{2T}}\right) \approx \left\langle N_F f_s^4(\boldsymbol{k})\right\rangle_{\text{FS}} \frac{7\zeta(3)}{16\pi^2T^2}. \quad \text{(B12)}$$

As a special case, one can obtain GL coefficients for local s-wave pairing derived by Gor'kov [5]. Considering $f_s = 1$, $f_d = 0$ we recover potential terms from Ref. [5].

APPENDIX C: DETAILS OF GINZBURG-LANDAU CALCULATIONS

GL parameters for points in Fig. 1 were calculated using Eqs. (B3) and (B10) within BCS approximation [like Eqs. (B11) and (B12)]. Averaging of form factors over Fermi surface is performed numerically. They are presented in Table I. Recall that coefficient $\beta_4 = \beta_3/4$.

It is convenient to rescale space (and simultaneously all GL coefficients) for numerical calculations. Total free energy in two dimensions has the form

$$\mathcal{F} = \int_{\mathcal{R}^2} F(x) d^2x, \quad \text{(C1)}$$

where $F(x)$ is given by Eq. (3). Performing space $x = \sqrt{\frac{\gamma_1}{|\alpha_1|}}x'$ and field $\Delta_{s/d}(x) = \sqrt{\frac{|\alpha_1|}{\beta_1}}\tilde{\Delta}_{s/d}(x')$,

TABLE I. Microscopically derived Ginzburg-Landau free-energy parameters for energy cutoff $\omega_D = 0.1$ for Eq. (3).

	Set 1	Set 2	Set 3	Units
Figure	3(a), 4, 6	3(b), 7	3(c)	
Ground state	$s + id$	s wave	d wave	
μ	1.665	1.673	1.665	t_{xy}
T	2.1	2.48	2.4	$\times 10^{-4} t_{xy}$
α_1	−13.07	−3.369	−2.185	$\times 10^{-3}$
α_2	−16.28	1.872	−5.321	$\times 10^{-3}$
β_1	6.829	4.982	5.229	$\times 10^{4}$
β_2	10.22	7.209	7.821	$\times 10^{4}$
β_3	2.749	1.972	2.104	$\times 10^{5}$
γ_1	2.571	1.857	1.969	$\times 10^{5}$
γ_2	2.257	1.604	1.728	$\times 10^{5}$
γ_{12}	1.374	0.9860	1.052	$\times 10^{5}$

$\tilde{\boldsymbol{A}}(x) = \frac{1}{q}\sqrt{\frac{|\alpha_1|}{\gamma_1}}\tilde{\boldsymbol{A}}'(x')$ rescaling one gets

$$\begin{aligned}\mathcal{F} = \frac{|\alpha_1|\gamma_1}{\beta_1}\int_{\mathcal{R}^2} d^2x' \Bigg[& \frac{\alpha_1}{|\alpha_1|}|\tilde{\Delta}_s|^2 + \frac{\alpha_2}{|\alpha_1|}|\tilde{\Delta}_d|^2 \\ & + |\tilde{\Delta}_s|^4 + \frac{\beta_2}{\beta_1}|\tilde{\Delta}_d|^4 + \frac{\beta_3}{\beta_1}|\tilde{\Delta}_s|^2|\tilde{\Delta}_d|^2 \\ & + \frac{\beta_4}{\beta_1}(\tilde{\Delta}_s^{*2}\tilde{\Delta}_d^2 + \tilde{\Delta}_s^2\tilde{\Delta}_d^{*2}) + |\boldsymbol{D}'\tilde{\Delta}_s|^2 + \frac{\gamma_2}{\gamma_1}|\boldsymbol{D}'\tilde{\Delta}_d|^2 \\ & + \frac{\gamma_{12}}{\gamma_1}[(D_y'\tilde{\Delta}_s)^*(D_y'\tilde{\Delta}_d) - (D_x'\tilde{\Delta}_s)^*(D_x'\tilde{\Delta}_d) + \text{c.c.}] \\ & + \frac{\kappa^2}{2}(\nabla' \times \tilde{\boldsymbol{A}}')^2\Bigg], \end{aligned} \quad \text{(C2)}$$

where $D_i' = \partial_i' + \tilde{A}_i'$ is a rescaled covariant derivative, $\kappa = \frac{\sqrt{\beta_1}}{\gamma_1 q}$. This form of free energy allows one to have all GL coefficients to be $O(1)$ that is convenient for numerical methods.

1. Coherence length for relative phase difference estimation

Let us consider the relative phase mode and ignore any mixed gradient couplings for simplicity, i.e., amplitudes of superconducting gaps are fixed. That is, we consider phase-difference-only fluctuations. Let us consider the fluctuation of the relative phase about the ground state,

$$\theta = \theta^{\text{GS}} + \phi, \quad \text{(C3)}$$

where the small fluctuation is ϕ. The linearized free energy with respect to ϕ is

$$F_{\text{lin}\phi} = F_{\text{GS}} + \frac{1}{2}K_{\text{rel}}(\varphi, \theta^{\text{GS}})(\nabla\phi)^2 + \frac{1}{2}\frac{\partial^2 F_p}{\partial\theta^2}\bigg|_{\theta=\theta^{\text{GS}}}\phi^2, \quad \text{(C4)}$$

where F_p is potential part of the free-energy equation (3),

$$K_{\rm rel}(\varphi,\theta) = \frac{2\left|\Delta_s^{\rm GS}\right|^2\left|\Delta_d^{\rm GS}\right|^2\left(\gamma_1\gamma_2-\gamma_{12}^2\cos^2 2\varphi\cos^2\theta\right)}{\gamma_1\left|\Delta_s^{\rm GS}\right|^2-2\gamma_{12}\left|\Delta_s^{\rm GS}\right|\left|\Delta_d^{\rm GS}\right|\cos 2\varphi\cos\theta+\gamma_2\left|\Delta_d^{\rm GS}\right|^2}. \tag{C5}$$

When substituting $\theta=\theta^{\rm GS}$, one gets

$$K_{\rm rel}(\varphi,\theta^{\rm GS}) = \frac{2\gamma_1\gamma_2\left|\Delta_s^{\rm GS}\right|^2\left|\Delta_d^{\rm GS}\right|^2}{\gamma_1\left|\Delta_s^{\rm GS}\right|^2+\gamma_2\left|\Delta_d^{\rm GS}\right|^2} \tag{C6}$$

and

$$\left.\frac{\partial^2 F_p}{\partial\theta^2}\right|_{\theta=\theta^{\rm GS}} = 2\beta_3\left|\Delta_s^{\rm GS}\right|^2\left|\Delta_d^{\rm GS}\right|^2. \tag{C7}$$

Therefore, coherence length for relative phase variations

$$\xi_\theta(\varphi) = a\sqrt{\frac{\gamma_1\gamma_2}{\beta_3\left(\gamma_1\left|\Delta_s^{\rm GS}\right|^2+\gamma_2\left|\Delta_d^{\rm GS}\right|^2\right)}} \tag{C8}$$

is independent of the direction φ. Note that it is defined in the region with two nucleated gap components ($s+id$ phase in our case) as can be seen in Fig. 2.

2. Numerical calculation details

After making rough estimates for length scales we can move to numerical solutions that allow to calculate length scales without these simplified estimates. The model consists of a two-component complex order parameter $\Delta_\alpha\in\mathbb{C}$ with $\alpha=1,2$ and a vector gauge field $\vec{\tilde{A}}=(\tilde{A}_1,\tilde{A}_2)\in\mathbb{R}^2$. We identify $\Delta_s=\Delta_1$ and $\Delta_d=\Delta_2$. Let the local coordinate be $x=(x_1,x_2)\in\mathbb{R}^2$ and define the local frame $\partial_j=\partial/\partial x_j$ for $j=1,2$. The GL energy density functional in index notation is

$$F = \frac{1}{2}\gamma_{jk}^{\alpha\beta}\overline{D_j\Delta_\alpha}D_k\Delta_\beta+\frac{\kappa^2}{2}|\vec{\nabla}\times\vec{\tilde{A}}|^2+F_p(\Delta_s,\Delta_d), \tag{C9}$$

where $\alpha,\beta,j,k=1,2$ and the gauge-covariant derivative is defined by the vector $\vec{D}=\vec{\nabla}+i\vec{\tilde{A}}$, and $\vec{\nabla}=(\partial_1,\partial_2)$ is the gradient operator. Note that we define

$$\overline{D_j\Delta_\alpha} = \partial_j\bar{\Delta}_\alpha-i\tilde{A}_j\bar{\Delta}_\alpha. \tag{C10}$$

The anisotropy matrices are given by

$$\gamma_{11} = 2\begin{pmatrix}\gamma_1 & -\gamma_{12}\\ -\gamma_{12} & \gamma_2\end{pmatrix},\quad \gamma_{22} = 2\begin{pmatrix}\gamma_1 & \gamma_{12}\\ \gamma_{12} & \gamma_2\end{pmatrix}. \tag{C11}$$

The potential energy we are considering is defined by

$$F_p(\Delta_s,\Delta_d) = \alpha_1|\Delta_s|^2+\alpha_2|\Delta_d|^2+\beta_1|\Delta_s|^4+\beta_2|\Delta_d|^4 + \beta_3|\Delta_s|^2|\Delta_d|^2+\beta_4\left(\Delta_s^2\bar{\Delta}_d^2+\bar{\Delta}_s^2\Delta_d^2\right). \tag{C12}$$

The associated static GL field equations are found to be

$$\frac{\delta F}{\delta\bar{\Delta}_\alpha} = \frac{\partial F_p}{\partial\bar{\Delta}_\alpha}-\frac{1}{2}\gamma_{ij}^{\alpha\beta}D_iD_j\Delta_\beta, \tag{C13a}$$

$$\frac{\delta F}{\delta\tilde{A}_i} = J_i+\kappa^2\partial_i\partial_j\tilde{A}_j-\kappa^2\partial_j\partial_j\tilde{A}_i. \tag{C13b}$$

where the supercurrent is

$$J_i = \frac{i}{2}\left(\gamma_{ji}^{\alpha\beta}\Delta_\beta\overline{D_j\Delta_\alpha}-\gamma_{ij}^{\beta\alpha}\bar{\Delta}_\beta D_j\Delta_\alpha\right). \tag{C14}$$

To obtain vortex solutions in our model, we must minimize the GL free-energy equation (C9). This amounts to solving the corresponding field equations (C13). We do this using an accelerated gradient descent method with flow arresting criteria. We reformulate the minimization as a second-order dynamical problem and solve the second-order system

$$\frac{{\rm d}^2\Delta_\alpha}{{\rm d}t^2} = \frac{1}{2}\gamma_{ij}^{\alpha\beta}D_iD_j\Delta_\beta-\frac{\partial F_p}{\partial\bar{\Delta}_\alpha}, \tag{C15}$$

$$\frac{{\rm d}^2\tilde{A}_i}{{\rm d}t^2} = \kappa^2\partial_j(\partial_j\tilde{A}_i-\partial_i\tilde{A}_j)-J_i, \tag{C16}$$

where t is a fictitious time. This system can then be reduced to a coupled first-order system, which we solve using a fourth-order Runge-Kutta method.

In order for our method to converge to a N-vortex solution, we need some appropriate initial configuration $\{\Delta_{s/d}(0),\vec{\tilde{A}}(0)\}=\{\Delta_{s/d}^0,\vec{A}^0\}$. For the superconducting order parameter, we use the ansatz

$$\Delta_\alpha^0 = \Delta_\alpha^{\rm GS}\sigma_\alpha(r)e^{iN_\alpha\theta_\alpha},\quad \vec{A}^0 = \frac{Na(r)}{r}(-\sin\theta,\cos\theta), \tag{C17}$$

where N_α is the vortex number in each component, N is the total vortex number, and $|\Delta_\alpha^{\rm GS}|$ is the ground-state value of the associated component. The total magnetic flux through the plane is given by

$$\Phi = 2\pi N,\quad N = \frac{\left|\Delta_s^{\rm GS}\right|^2N_s+\left|\Delta_d^{\rm GS}\right|^2N_d}{\left|\Delta_s^{\rm GS}\right|^2+\left|\Delta_d^{\rm GS}\right|^2}. \tag{C18}$$

The profile functions are monotonically increasing functions that satisfy the boundary conditions $\sigma_\alpha(0)=a(0)=0$ and

$$\lim_{r\to\infty}\sigma_\alpha(r) = \lim_{r\to\infty}a(r) = 1. \tag{C19}$$

Note that in general boundary conditions are more subtle [49]. However, we choose simulation box large enough so that there is no vortex interaction with boundaries within numerical accuracy. Hence, the simplest boundary conditions are sufficient for our case.

For our initial configuration, we simply set $\sigma_\alpha(r)=a(r)=\tanh(r)$.

3. Skyrmions

When integer flux vortices split into spatially separated fractional vortices in each component Δ_α, such that their cores (zeros of the components $\Delta_\alpha=0$) are never coincident, skyrmions form. That can be seen by representing superconducting gap fields in terms of a pseudospin vector [50]. For such structures, one may construct a gauge-invariant field $\phi:\mathbb{R}^2\to S^2$, given by

$$\phi = \frac{1}{|\Delta_s|^2+|\Delta_d|^2}\begin{pmatrix}\Delta_s^*\Delta_d+\Delta_s\Delta_d^*\\ i(\Delta_s^*\Delta_d-\Delta_s\Delta_d^*)\\ |\Delta_d|^2-|\Delta_s|^2\end{pmatrix}. \tag{C20}$$

The field ϕ is convenient to illustrate using standard Runge coloring scheme [26] (as shown in Fig. 7). We can describe

the skyrmion field using the gauge-invariant quantities Δ, $\rho = \sqrt{|\Delta_s|^2 + |\Delta_d|^2}$, and the supercurrent J, where we are regarding the supercurrent as a 1-form on $\mathbb{R}^2$. We can express the magnetic field (as a 2-form on $\mathbb{R}^2$) in terms of these gauge-invariant quantities as [27,51]

$$B = \frac{1}{2}\phi^*\omega - \mathrm{d}\left(\frac{J}{\rho^2}\right), \tag{C21}$$

where ω is the usual area form on the target S^2 and d is the exterior derivative. Then, using Stoke's theorem, we observe that the skyrmion number is precisely the number of magnetic flux quanta in the field configuration, that is,

$$\int_{\mathbb{R}^2} B = \frac{1}{2}\int_{\mathbb{R}^2} \phi^*\omega = 2\pi\, \mathcal{Q}(\phi). \tag{C22}$$

[1] V. L. Ginzburg, Nobel lecture: On superconductivity and superfluidity (what I have and have not managed to do) as well as on the "physical minimum" at the beginning of the XXI century, Rev. Mod. Phys. **76**, 981 (2004).

[2] A. Larkin and A. Varlamov, *Theory of Fluctuations in Superconductors* (Oxford University Press, Oxford, 2005), Vol. 127.

[3] L. Landau and V. Ginzburg, K teorii sverkhrovodimosti, Zh. Eksp. Teor. Fiz **20**, 546 (1950).

[4] A. A. Abrikosov, Magnetic properties of superconductors of the second group, Zh. Eksp. Teor. Fiz. **32**, 1442 (1957) [Sov. Phys. –JETP **5**, 1174 (1957)].

[5] L. P. Gor'kov, Microscopic derivation of the Ginzburg-Landau equations in the theory of superconductivity, Zh. Eksp. Teor. Fiz. **36**, 1918 (1959) [Sov. Phys.–JETP **9**, 1364 (1959)].

[6] J. Carlström, J. Garaud, and E. Babaev, Length scales, collective modes, and type-1.5 regimes in three-band superconductors, Phys. Rev. B **84**, 134518 (2011).

[7] J. Garaud, A. Corticelli, M. Silaev, and E. Babaev, Properties of dirty two-band superconductors with repulsive interband interaction: Normal modes, length scales, vortices, and magnetic response, Phys. Rev. B **98**, 014520 (2018).

[8] V. Moshchalkov, M. Menghini, T. Nishio, Q. H. Chen, A. V. Silhanek, V. H. Dao, L. F. Chibotaru, N. D. Zhigadlo, and J. Karpinski, Type-1.5 superconductivity, Phys. Rev. Lett. **102**, 117001 (2009).

[9] E. Babaev and M. Speight, Semi-Meissner state and neither type-I nor type-II superconductivity in multicomponent superconductors, Phys. Rev. B **72**, 180502(R) (2005).

[10] J. Carlström, E. Babaev, and M. Speight, Type-1.5 superconductivity in multiband systems: Effects of interband couplings, Phys. Rev. B **83**, 174509 (2011).

[11] M. Silaev and E. Babaev, Microscopic theory of type-1.5 superconductivity in multiband systems, Phys. Rev. B **84**, 094515 (2011).

[12] M. Silaev and E. Babaev, Microscopic derivation of two-component Ginzburg-Landau model and conditions of its applicability in two-band systems, Phys. Rev. B **85**, 134514 (2012).

[13] I. Timoshuk and E. Babaev, Microscopic solutions for vortex clustering in two-band type-1.5 superconductors, Phys. Rev. B **110**, 064509 (2024).

[14] T. Nishio, V. H. Dao, Q. Chen, L. F. Chibotaru, K. Kadowaki, and V. V. Moshchalkov, Scanning SQUID microscopy of vortex clusters in multiband superconductors, Phys. Rev. B **81**, 020506(R) (2010).

[15] S. J. Ray, A. S. Gibbs, S. J. Bending, P. J. Curran, E. Babaev, C. Baines, A. P. Mackenzie, and S. Lee, Muon-spin rotation measurements of the vortex state in Sr_2RuO_4: Type-1.5 superconductivity, vortex clustering, and a crossover from a triangular to a square vortex lattice, Phys. Rev. B **89**, 094504 (2014).

[16] P. K. Biswas, F. N. Rybakov, R. P. Singh, S. Mukherjee, N. Parzyk, G. Balakrishnan, M. R. Lees, C. D. Dewhurst, E. Babaev, A. D. Hillier, *et al.*, Coexistence of type-I and type-II superconductivity signatures in ZrB_{12} probed by muon spin rotation measurements, Phys. Rev. B **102**, 144523 (2020).

[17] Y. Wang, H. Yao, T. Winyard, C. Broyles, S. Gould, Q. He, K. Liang, Z. Li, P. Zhang, B. Chen, K. Yao, Q. Zhou, J. Zhu, B. Xiang, D. Agterberg, E. Babaev, S. Ran, and Y. Wang, Observation of vortex stripes in UTe_2, Nano Lett. **25**, 12824 (2025).

[18] Y. Ren, J.-H. Xu, and C. S. Ting, Ginzburg-Landau equations for mixed s+d symmetry superconductors, Phys. Rev. B **53**, 2249 (1996).

[19] K. A. Musaelian, J. Betouras, A. V. Chubukov, and R. Joynt, Mixed-symmetry superconductivity in two-dimensional Fermi liquids, Phys. Rev. B **53**, 3598 (1996).

[20] H. Shimahara, Stability of mixed-symmetry superconducting states with broken time-reversal symmetry against lattice distortions, J. Phys. Soc. Jpn. **90**, 064711 (2021).

[21] E. Babaev, J. Carlström, and M. Speight, Type-1.5 superconducting state from an intrinsic proximity effect in two-band superconductors, Phys. Rev. Lett. **105**, 067003 (2010).

[22] M. Speight, T. Winyard, A. Wormald, and E. Babaev, Magnetic field behavior in $s + is$ and $s + id$ superconductors: Twisting of applied and spontaneous fields, Phys. Rev. B **104**, 174515 (2021).

[23] T. Winyard, M. Silaev, and E. Babaev, Hierarchies of length-scale based typology in anisotropic U(1) s-wave multiband superconductors, Phys. Rev. B **99**, 064509 (2019).

[24] M. Rotter, M. Pangerl, M. Tegel, and D. Johrendt, Superconductivity and crystal structures of $Ba_{1-x}K_xFe_2As_2 (x = 0 - 1)$, Angew. Chem. Int. Ed. **47**, 7949 (2008).

[25] J. Carlström, J. Garaud, and E. Babaev, Semi-Meissner state and nonpairwise intervortex interactions in type-1.5 superconductors, Phys. Rev. B **84**, 134515 (2011).

[26] P. Leask, Baby skyrmion crystals, Phys. Rev. D **105**, 025010 (2022).

[27] J. Garaud, J. Carlström, E. Babaev, and M. Speight, Chiral $\mathbb{C}P^2$ skyrmions in three-band superconductors, Phys. Rev. B **87**, 014507 (2013).

[28] Y. Zheng, Q. Hu, X. Yu, H. Ji, I. Timoshuk, J. Garaud, H. Xu, Y. Li, Y. Gao, X. Yu, V. Grinenko *et al.*, Observation of quantum vortex core fractionalization and skyrmion formation in a superconductor, Science **0**, eads0189 (2026).

[29] L.-F. Zhang, Y.-Y. Zhang, G.-Q. Zha, M. V. Milošević, and S.-P. Zhou, Skyrmionic chains and lattices in $s + id$ superconductors, Phys. Rev. B **101**, 064501 (2020).

[30] J. Garaud, J. Carlström, and E. Babaev, Topological solitons in three-band superconductors with broken time reversal symmetry, Phys. Rev. Lett. **107**, 197001 (2011).

[31] H. Weber, M. Botlo, F. Sauerzopf, H. Wiesinger, and U. Klein, Phase transitions between type-I, type-II/1 and type-II/2 superconductivity, Jpn. J. Appl. Phys. **26**, 917 (1987).

[32] W. Wang, R. Díaz-Méndez, M. Wallin, J. Lidmar, and E. Babaev, Pinning effects in a two-dimensional cluster glass, Phys. Rev. B **104**, 144206 (2021).

[33] L. Bauer, D. He, S. Bharadwaj, S. Liu, P. V. Balachandran, and Z. Jacob, Type-1.5 SNSPD: Interacting vortex theory of two bandgap superconducting single photon detectors, Appl. Phys. Lett. **127**, 122603 (2025).

[34] https://github.com/Paulnleask/soliton_solver.

[35] J. Bardeen, L. N. Cooper, and J. R. Schrieffer, Theory of superconductivity, Phys. Rev. **108**, 1175 (1957).

[36] J. Hu and H. Ding, Local antiferromagnetic exchange and collaborative Fermi surface as key ingredients of high temperature superconductors, Sci. Rep. **2**, 381 (2012).

[37] T. Xiang and C. Wu, *D-wave Superconductivity* (Cambridge University Press, Cambridge, 2022).

[38] E. Shapoval, On the phase transition $d \to (s \pm id)$ in high-T_c superconductors, J. Exp. Theor. Phys. Lett. **64**, 625 (1996).

[39] M. Liu, D. Y. Xing, and Z. D. Wang, Mixed $(s + id)$-wave order parameters in the Van Hove scenario, Phys. Rev. B **55**, 3181 (1997).

[40] A. Ghosh and S. K. Adhikari, Two phase transitions in $(d_{x^2-y^2} + is)$-wave superconductors, Phys. C (Amsterdam) **322**, 37 (1999).

[41] H. S. Røising, G. Wagner, M. Roig, A. T. Rømer, and B. M. Andersen, Heat capacity double transitions in time-reversal symmetry broken superconductors, Phys. Rev. B **106**, 174518 (2022).

[42] S. Maiti and P. J. Hirschfeld, Collective modes in superconductors with competing s- and d-wave interactions, Phys. Rev. B **92**, 094506 (2015).

[43] S. Ghosh, M. S. Ikeda, A. R. Chakraborty, T. Worasaran, F. Theuss, L. B. Peralta, P. Lozano, J.-W. Kim, P. Thompson, P. J. Ryan, *et al.*, Elastocaloric evidence for a multicomponent superconductor stabilized within the nematic state in $Ba(Fe_{1-x}Co_x)_2As_2$, Proc. Natl. Acad. Sci. USA **122**, e2424833122 (2025).

[44] M. Timirgazin, V. Gilmutdinov, and A. Arzhnikov, Phase diagrams of singlet superconducting states with mixed symmetry, Phys. C (Amsterdam) **557**, 7 (2019).

[45] A. Talkachov and E. Babaev, Microscopic theory of strain-controlled split superconducting and time-reversal symmetry breaking transitions in $s + id$ superconductors, Phys. Rev. B **113**, 144515 (2026).

[46] A. C. Yuan, E. Berg, and S. A. Kivelson, Strain-induced time reversal breaking and half quantum vortices near a putative superconducting tetracritical point in Sr_2RuO_4, Phys. Rev. B **104**, 054518 (2021).

[47] K. Kuboki and K. Yano, Microscopic derivation of Ginzburg–Landau equations for coexistent states of superconductivity and magnetism, J. Phys. Soc. Jpn. **81**, 064711 (2012).

[48] D. L. Feder and C. Kallin, Microscopic derivation of the Ginzburg-Landau equations for a d-wave superconductor, Phys. Rev. B **55**, 559 (1997).

[49] A. Samoilenka and E. Babaev, Microscopic derivation of superconductor-insulator boundary conditions for Ginzburg-Landau theory revisited: Enhanced superconductivity at boundaries with and without magnetic field, Phys. Rev. B **103**, 224516 (2021).

[50] E. Babaev, L. D. Faddeev, and A. J. Niemi, Hidden symmetry and knot solitons in a charged two- condensate Bose system, Phys. Rev. B **65**, 100512(R) (2002).

[51] T. Winyard, M. Silaev, and E. Babaev, Skyrmion formation due to unconventional magnetic modes in anisotropic multiband superconductors, Phys. Rev. B **99**, 024501 (2019).